J. Fluid Mech. (2025), *vol.* 1004, A9, doi:10.1017/jfm.2024.1103

Laminar flow over I-shaped dual-step cylinders

Cai Tian[1], **Jianxun Zhu**[1,†], **Helge I. Andersson**[1], **Bjørnar Pettersen**[1] **and Lars Erik Holmedal**[1]

[1]Department of Marine Technology, Norwegian University of Science and Technology (NTNU), NO-7491 Trondheim, Norway

(Received 7 March 2024; revised 7 November 2024; accepted 13 November 2024)

The three-dimensional flow field past an I-shaped dual-step cylinder has been obtained by numerical integration of the Navier–Stokes equations at Reynolds number (Re_D) 150. The I-shaped cylinder consisted of two large-diameter (D) cylinders with a small-diameter (d) cylinder in between. With a view to exploring the vortex dynamics and structural loads, simulations were performed for eight different lengths l of the small cylinder, varied from $l/D = 10$ to 0.2 for a fixed diameter ratio $D/d = 2$. When the length of the small cylinder is sufficiently large, the wake behind the I-shaped cylinder is similar to the wake behind the single-step cylinder (Tian *et al.*, *J. Fluid Mech.*, vol. 891, 2020, A24). As the small cylinder length decreases, the enhanced interactions between the two steps make the present wake deviate from the wake of the single-step cylinder, leading to four different wake modes distinguished by different combinations of vortex cells. The physical formation mechanisms were analysed in terms of the vortex dynamics. Besides the wake flow, the streamwise vortices around the I-shaped step cylinder were also investigated. A pair of edge vortices and a junction vortex were identified for $l/D \geq 1$. When the gap between the two steps becomes too small, $l/D \leq 0.2$, the junction vortex disappears, and only a pair of edge vortices exists. Varying the distance between the two steps strongly affects the structural loads (drag and lift) along the I-shaped cylinder. The dependence of the loads on l/D was readily explained by the different wake modes.

Key words: vortex dynamics, wakes, vortex shedding

1. Introduction

A cylindrical geometry with abrupt changes in its diameter (sketched in figure 1*a* and referred to as the multi-step cylinder) has attracted attention recently due to its many practical applications, such as steel lazy wave risers (Yin, Lie & Wu 2020), heat exchangers (Jayavel & Tiwari 2009) and bridge cables (Matsumoto, Shiraishi & Shirato 1992), as

† Email address for correspondence: jianxun.zhu@ntnu.no

© The Author(s), 2025. Published by Cambridge University Press. This is an Open Access article, distributed under the terms of the Creative Commons Attribution-NonCommercial licence (http://creativecommons.org/licenses/by-nc/4.0), which permits non-commercial re-use, distribution, and reproduction in any medium, provided the original article is properly cited. The written permission of Cambridge University Press must be obtained prior to any commercial use.

https://doi.org/10.1017/jfm.2024.1103 Published online by Cambridge University Press

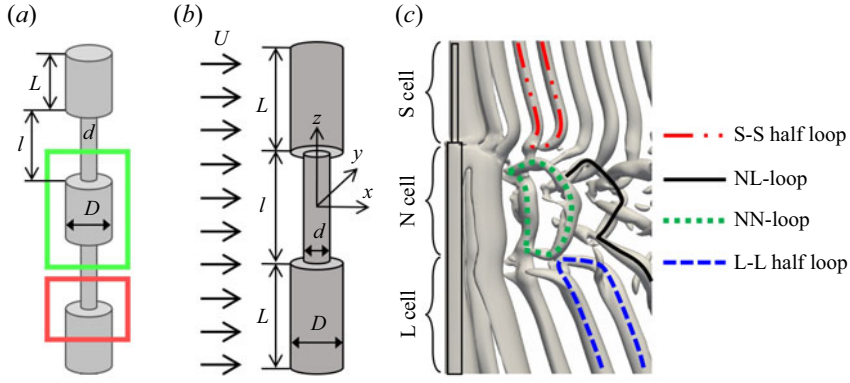

Figure 1. (*a*) A sketch of the multi-step cylinder. The red and green rectangles mark the single-step and the dual-step cylinders, respectively. (*b*) The configuration investigated in the present manuscript: the I-shaped step cylinder. The diameters of the small and large cylinders are d and D, respectively, l is the length of the small cylinder and L is the length of the large cylinder. The origin is located in the middle of the small cylinder. The uniform incoming flow U is in the positive x-direction. The three directions are named the streamwise (x-direction), cross-flow (y-direction) and spanwise (z-direction) directions. (*c*) Instantaneous wake behind a step cylinder with $D/d = 2$ at $Re_D = 150$, taken at the moment when vortex dislocations occur. The wake structures are shown by the isosurfaces of $\lambda_2 = -0.05$ (Jeong & Hussain 1995) from Tian *et al.* (2023). The coloured curves on the isosurfaces indicate the different vortex structures.

well as its potential application in structural load optimizations (Nakamura & Igarashi 2008). The flow characteristics around a multi-step cylinder are complicated and depend on the diameter ratio (D/d) between the large-diameter (D) and the small-diameter (d) cylinders, the Reynolds numbers ($Re_D = UD/\nu$, where U is the free-stream velocity and ν is the kinematic viscosity of the fluid), the length of the large cylinder(s) L and the length of the small cylinder(s) l. Previous research has studied the effects of D/d and L on the flow characteristics separately based on the single-step cylinder (Lewis & Gharib 1992; Dunn & Tavoularis 2006; Morton & Yarusevych 2010, 2014*b*; Massaro, Peplinski & Schlatter 2023*b*; Tian *et al.* 2023; Zhao & Zhang 2023), marked by the red rectangle in figure 1(*a*), and the dual-step cylinder (Morton & Yarusevych 2014*a*; Ji *et al.* 2020; Morton & Yarusevych 2020; Yu, Ji & Srinil 2020; Bulbule, Kumar & Singh 2024; Theja *et al.* 2024), marked by the green rectangle in figure 1(*a*). However, how the gap between two steps affects the flow (i.e. how the flow changes over I-shaped step cylinders with varying lengths of the small cylinder) has rarely been investigated in detail. The purpose of the present paper is to fill in some of this knowledge gap by investigating the flow over an I-shaped dual-step cylinder (sketched in figure 1*b*) for different l, which can serve as a stepping stone for understanding the flow over a multi-step cylinder.

As shown in figure 1(*b*,*c*), an I-shaped step cylinder can be treated as a combination of two single-step cylinders. Although the potential interactions between the two steps can complicate the wake flow, it is worth reviewing previous literature on the single-step cylinder first. In 1992, Lewis & Gharib (1992) identified two wake modes by experimentally investigating the flow over a single-step cylinder with $1.14 < D/d < 1.76$ at $67 < Re_D < 200$; an indirect mode for $D/d > 1.55$ and a direct mode for $D/d < 1.25$ were observed. In the direct mode, two dominant vortices shed from the small and large cylinders, exhibiting two shedding frequencies: f_S behind the small cylinder and f_L behind the large cylinder. These two vortices directly interact with each other. For the indirect mode, the direct interaction between the vortices with f_S and f_L disappears due to another vortex occurring between them with a shedding frequency f_3 (also referred to

https://doi.org/10.1017/jfm.2024.1103 Published online by Cambridge University Press

as f_N in Dunn & Tavoularis 2006). The majority of the following studies have focused on the indirect mode. Dunn & Tavoularis (2006) conducted experiments for flow over a single-step cylinder with $D/d \approx 2$ at $63 < Re < 1100$, where three spanwise vortex cells (i.e. the vortex cells with the dominant vorticity component in the spanwise direction) were identified for the indirect mode: (i) the S-cell vortex shedding from the small cylinder with the largest shedding frequency f_S, (ii) the L-cell vortex behind the large cylinder with the smallest shedding frequency f_L and (iii) the N-cell vortex shedding from the large cylinder with the shedding frequency f_N, located between the S- and L-cell vortices. An example of these three vortices are shown in figure 1(*c*). Dunn & Tavoularis (2006), Morton & Yarusevych (2010) and Tian *et al.* (2020*a*) found that the formation of the N-cell vortex is closely related to the joint effects of both the axial velocity induced by the step along the large cylinder and the increased base pressure on the large cylinder near the step. Massaro & Schlatter (2024) conducted the first global stability analysis of the flow over single-step cylinder with $1.1 \leq D/d \leq 4$ at $Re_D = 40$, 50 and 80, revealing three supercritical Hopf bifurcations responsible for the three dominant vortex cells (i.e. the N, S and L cells).

Most of the vortex interactions in the step cylinder wake flow are closely related to a flow phenomenon denoted vortex dislocation, which will be described as follows. The concept of 'vortex dislocation' was first introduced by Williamson (1989), adopting the idea from solid mechanics. In an experiment of the wake behind a circular cylinder with two end plates, Williamson (1989) used the phrase 'vortex dislocation' to describe the neighbouring vortices periodically moving out of phase due to their different shedding frequencies. Behind the single-step cylinder, vortex dislocations form both at the boundary between the S- and N-cell vortices and at the boundary between the N- and L-cell vortices. Lewis & Gharib (1992) first found that the vortex dislocations between the S- and N-cell vortices occur within a time-invariant narrow region, slightly deflecting spanwise into the large cylinder side just behind the step. This observation was confirmed by Dunn & Tavoularis (2006) and Morton & Yarusevych (2010). Morton & Yarusevych (2010) conducted numerical simulations of flow over a single-step cylinder with $D/d = 2$ at $Re_D = 150$ and 300. They discovered that the connections between the S- and N-cell vortices depend on the frequency ratio f_S/f_N, and that the S-N dislocation exhibits a beat frequency $f_S - f_N$ with the formation of the SS-half loop vortex structure (shown in figure 1*c*). The interactions between the N- and L-cell vortices were numerically investigated by Morton & Yarusevych (2010) and Tian *et al.* (2017*a*,*b*, 2019, 2020*b*) for a single-step cylinder with $2 < D/d < 3$ at $Re_D = 150$. The authors found that the shape and the spanwise length of the N-cell vortices, as well as the position of the N-L cell boundary, change periodically as the vortex dislocation between the N- and L-cell vortices occurs at the beat frequency $f_L - f_N$. The NL-loop, NN-loop and LL-half loop vortex structures (shown in figure 1*c*) were identified during the N-L dislocation process. These vortex-loop structures were mainly discovered in the laminar flow regime; however, they seem to persist as Re_D increases. Recently, Massaro *et al.* (2023*b*) captured the SS-, NL- and LL-loop structures in direct numerical simulations of flow over a single-step cylinder with $D/d = 2$ at $Re_D = 1000$ by reconstructing wake flows via proper orthogonal decomposition on the most energetic modes. Besides the dominant vortices in the wake, the vortices generated around the step were investigated numerically by Tian *et al.* (2021), Massaro, Peplinski & Schlatter (2023*a*), Massaro *et al.* (2023*b*) and experimentally by Dunn & Tavoularis (2006), where the horseshoe-like junction vortices and tip vortices were identified. The flow around a rotating single-step cylinder in the laminar regime was recently first investigated by Zhao & Zhang (2023).

https://doi.org/10.1017/jfm.2024.1103 Published online by Cambridge University Press

The structural load characteristics of the single-step cylinder were first experimentally investigated by Ko & Chan (1984) for $D/d = 2$ at $Re_D = 80\,000$. The authors found that the drag force coefficient gradually decreases along the small cylinder while increasing along the large cylinder as the step is approached due to the disturbance of the step. Similar results were observed by Tian *et al.* (2023) and Morton, Yarusevych & Carvajal-Mariscal (2009) by numerical simulation of a single-step cylinder with $D/d = 2$ at $Re_D = 150$ and 2000. Tian *et al.* (2023) provided a detailed discussion of how vortex interactions in the wake affect the spanwise variation of the structural loads along the single-step cylinder. They found that the formation of vortex dislocations can cause a major reduction (90 %) of the local lift amplitude and a relatively modest reduction (5.7 %) of the local drag amplitude (the corresponding formula can be found in § 5). Three minima on the drag and lift distributions were identified and ascribed to the effects of the vortex dislocation and the disturbance from the step.

The primary goal of the present numerical study is to (i) investigate how the flow develops over an I-shaped step cylinder; (ii) study how the length of the small cylinder (l) affects the development of the wake flow; (iii) investigate the structural loads distribution along the I-shaped step cylinder. To achieve this, we analyse the results obtained from direct numerical simulations (DNS) of the flow past eight different I-shaped step cylinders with $D/d = 2$ and $l/D = 10$, 5, 3, 2.5, 2, 1.5, 1 and 0.2. The Reynolds number for the large cylinder (Re_D) is set to 150 to avoid interference of three-dimensional wake instabilities, such as the elliptical instability and the natural vortex dislocation, which occur at $Re_D \approx 180$ in the wake of a uniform circular cylinder.

The paper is organized as follows: § 2 describes the flow configuration and the numerical settings. In § 3, four distinct wake patterns are identified behind the I-shaped step cylinder as the length of the small cylinder l changes from $10D$ to $0.2D$. Section 4 describes the streamwise vortices around the I-shaped step cylinder. In § 5, the structural load distribution along the I-shaped step cylinder is analysed for different wake patterns.

2. Governing equations, boundary conditions and convergence study

A sketch of the I-shaped step cylinder is plotted in figure 1(*b*), showing that the origin of the coordinate system is in the middle of the small cylinder. The uniform incoming flow U is in the positive x-direction. The diameter ratio D/d of the I-shaped step cylinder is fixed at 2.0. The length of the small cylinder is given as $l/D = 10$, 5, 3, 2.5, 2, 1.5, 1 and 0.2. The governing equations for the incompressible flow are the continuity equation and the time-dependent three-dimensional incompressible Navier–Stokes equation

$$\nabla \cdot \boldsymbol{u} = 0, \tag{2.1}$$

$$\frac{\partial \boldsymbol{u}}{\partial t} + (\boldsymbol{u} \cdot \nabla)\boldsymbol{u} = \frac{1}{Re}\nabla^2 \boldsymbol{u} - \nabla p, \tag{2.2}$$

where $\boldsymbol{u}$ is the velocity vector and p is the pressure, while ρ and t denote the fluid density and time, respectively. The velocity, pressure, time and length are scaled by U, ρU^2, D/U and D.

Direct numerical simulations were conducted by using the finite-volume numerical code MGLET (Manhart 2004). Previous studies have thoroughly validated this code for various applications, for example, the flow around step cylinders (Tian *et al.* 2020*b*, 2021, 2023), the flow around a prolate spheroid (Jiang *et al.* 2018), the flow around a cylinder–wall junction (Schanderl *et al.* 2017) and the oscillatory flow through a hexagonal sphere pack (Unglehrt & Manhart 2022). A staggered numerical grid is used, where the pressure

https://doi.org/10.1017/jfm.2024.1103 Published online by Cambridge University Press

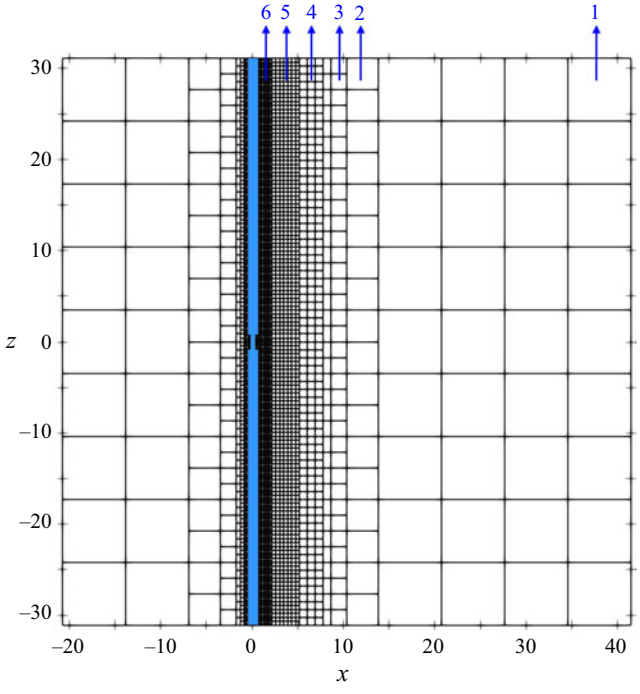

Figure 2. An illustration of the multi-level grids in the xz-plane at $y = 0$ for $l/D = 2$. Each square represents a slice of the corresponding cubic Cartesian grid box that contains $N \times N \times N$ grid cells. Here, there are six levels of grid boxes as indicated by the numbers.

is evaluated in the middle of the grid boundaries and the velocities are located in the middle of the grid face. The midpoint rule is applied to approximate the surface integral, leading to second-order accuracy. A third-order Runge–Kutta scheme (Williamson 1980) is applied for the time integration. The time step Δt is equal to 0.003, ensuring a Courant–Friedrichs–Lewy number smaller than 0.5 for all simulations in the present study. The elliptic pressure correction equation is solved by Stone's implicit procedure (Stone 1968). The I-shaped step cylinder geometry is handled by an immersed boundary method (Peller *et al.* 2006; Peller 2010).

Figure 2 schematically illustrates the grid structure in the symmetry plane (the xz-plane at $y = 0$) for the I-shaped step cylinder with $l/D = 2$. The zonally embedded grid method (Manhart 2004) is applied for building the grid. The computational domain is first equally divided into cubic grid boxes, called the level-1 box. Each grid box contains $N \times N \times N$ equally sized cubic grid cells. The local grid refinement is achieved by continuously dividing the grid box (the level-1 box) into eight smaller grid boxes, denoted the level-2 box. Each level-2 box also contains $N \times N \times N$ equally sized cubic grid cells. This grid-refinement process continues until the finest specified grid level is reached (all simulations in this study have six grid levels). The size of the grid-refinement region was checked to ensure that it is sufficiently large for reliable DNS simulations in the present study. The treatment and validation of the zonally multi-grid hierarchical solution can be found in Manhart (2004).

Figure 3 shows the side and top-down views of the flow domain. The streamwise length of the flow domain is L_x, where L_{x1} and L_{x2} are the distance from the inlet and outlet planes to the centre of the step cylinder, respectively. The cross-flow length of

https://doi.org/10.1017/jfm.2024.1103 Published online by Cambridge University Press

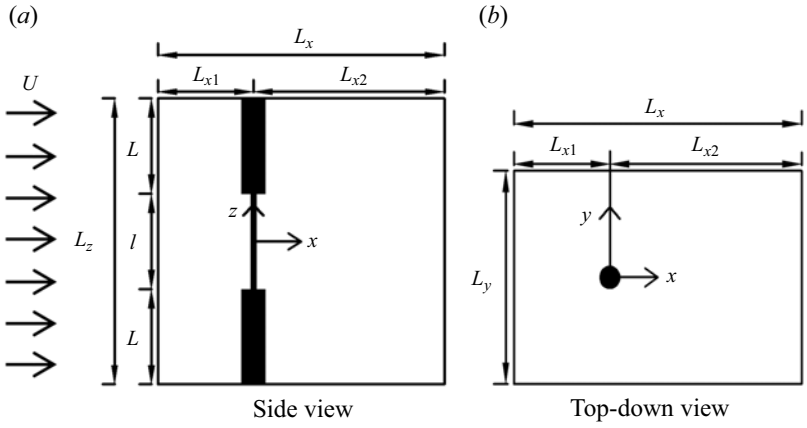

Figure 3. Computational domain and coordinate system are illustrated from (*a*) side view and (*b*) top-down view.

Wake mode	F3SNL	F2MNL	F3MNL	F1L
l/D	10, 5, 3	2.5, 2	1.5, 1	0.2
Vortex cell	S cell	M cell	M cell	L cell
	N cell	N cell	N cell	
	L cell	L cell	L cell	
Dominant frequency	$St_S > St_L > St_N$	$St_L > St_M = St_N$	$St_M > St_L > St_N$	St_L

Table 1. An overview of four wake modes, the dominant vortex cells and the relative magnitude between the corresponding Strouhal numbers (St): S cell, $St_S = f_S D/U$; M cell, $St_M = f_M D/U$; N cell, $St_N = f_N D/U$; L cell, $St_L = f_L D/U$.

the flow domain is L_y, where the I-shaped step cylinder is located in the middle. The spanwise height of the domain is L_z, where the length of the small and large cylinders is l and L, respectively. A constant and uniform velocity profile ($u = U$ and $v = w = 0$) is applied at the inlet. No numerical noise is applied at the inlet. A Neumann condition ($\partial u/\partial x = \partial v/\partial x = \partial w/\partial x = 0$) is applied at the outlet. For the other four sides of the computational domain, a free-slip boundary condition is applied (for the two vertical sides $v = 0$, $\partial u/\partial y = \partial w/\partial y = 0$; for the two horizontal sides: $w = 0$, $\partial u/\partial z = \partial v/\partial z = 0$). A no-slip and no-penetration condition ($u = v = w = 0$) is imposed at the step cylinder surface. Neumann conditions are applied for the pressure, except at the outlet where the pressure is set equal to zero.

Table 1 shows an overview over all the simulations conducted in the present work. The length of the small cylinder varies from $0.2D$ to $10D$. More detailed information of the flow domain and a grid convergence study are described in Appendix A.

3. Wake topology

The I-shaped step cylinder depicted in figure 1(*b*) contains two steps. When the distance between these two steps varies from $10D$ to $0.2D$, four distinctly different wake modes are newly identified behind the I-shaped step cylinder with $D/d = 2$ at $Re_D = 150$. An overview of these four wake modes is summarized in table 1; the corresponding vortex structures and the frequency spectra are shown in figures 4 and 5, respectively.

https://doi.org/10.1017/jfm.2024.1103 Published online by Cambridge University Press

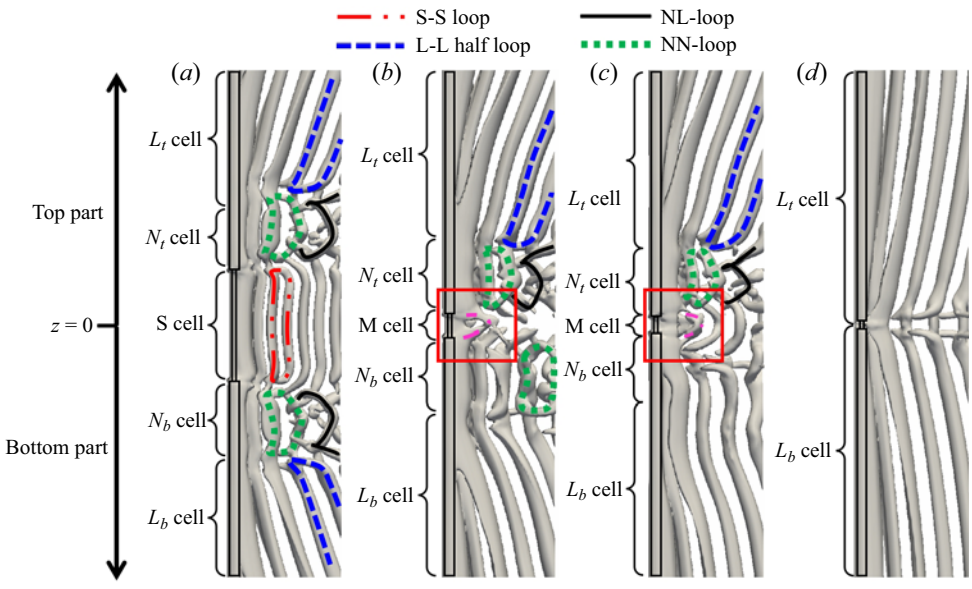

Figure 4. Instantaneous isosurfaces of $\lambda_2 = -0.01$ for (*a*) $l/D = 10$, (*b*) $l/D = 2$, (*c*) $l/D = 1.5$ and (*d*) $l/D = 0.2$. The coloured curves on the isosurfaces indicate the different vortex structures. The parts of the I-shaped step cylinder at $z > 0$ and $z < 0$ are referred to as the top and bottom parts, respectively.

The topology of vortices is visualized by isosurfaces of $\lambda_2 = -0.01$ (Jeong & Hussain 1995). The wake vortex cells for the single-step cylinder flow were classified by distinct vortex shedding frequencies (Dunn & Tavoularis 2006). However, the flow interactions triggered by the two steps of the present I-shaped step cylinder induce a more complex wake flow compared with the single-step cylinder wake. As a result, the classification of the wake cells in the present I-shaped step cylinder flow is based on a combination of the vortex shedding frequency and the vortex topology. If the two steps of an I-shaped step cylinder are sufficiently far away from each other (i.e. l is large enough), three dominant vortex cells occur, the S-cell vortex, N-cell vortex and L-cell vortex (figure 4*a*) with three distinct shedding frequencies (figure 5*a*). This mode, which is observed for $l/D = 10$, 5, 3, is denoted the F3SNL mode (i.e. where 3 denotes the number of dominant shedding frequencies and SNL denotes the corresponding vortex cells). Since the topology and formation mechanism (as will be further discussed in the following subsections) of these three dominant vortices behind the I-shaped dual-step cylinder are similar to those behind the single-step cylinder, the names of these three dominant vortices are adopted from the single-step cylinder wake (Dunn & Tavoularis 2006), as shown in figure 1(*c*) and described in the introduction. When the distance l between the two steps (l) decreases, the three-dimensional wakes induced by these two steps start interacting, causing three other wake modes. The second wake mode, which is observed for $l/D = 2.5$ and 2, is denoted the F2MNL mode, where three dominant vortex cells, the M-, N- and L-cell vortices, occur (figure 4*b*) with two dominant shedding frequencies (figure 5*b*). Here, the S-cell vortex disappears as the length of the small cylinder decreases. Instead, we identify a new vortex cell, the M cell, in the middle of the I-shaped step cylinder wake. Although the M cell and the N cell have the same shedding frequency, they have distinct vortex topologies, which will be discussed in detail in § 3.2. The third wake mode, which is observed for $l/D = 1.5$ and 1, is denoted the F3MNL mode. Similar to the F2MNL mode, three dominant vortex

https://doi.org/10.1017/jfm.2024.1103 Published online by Cambridge University Press

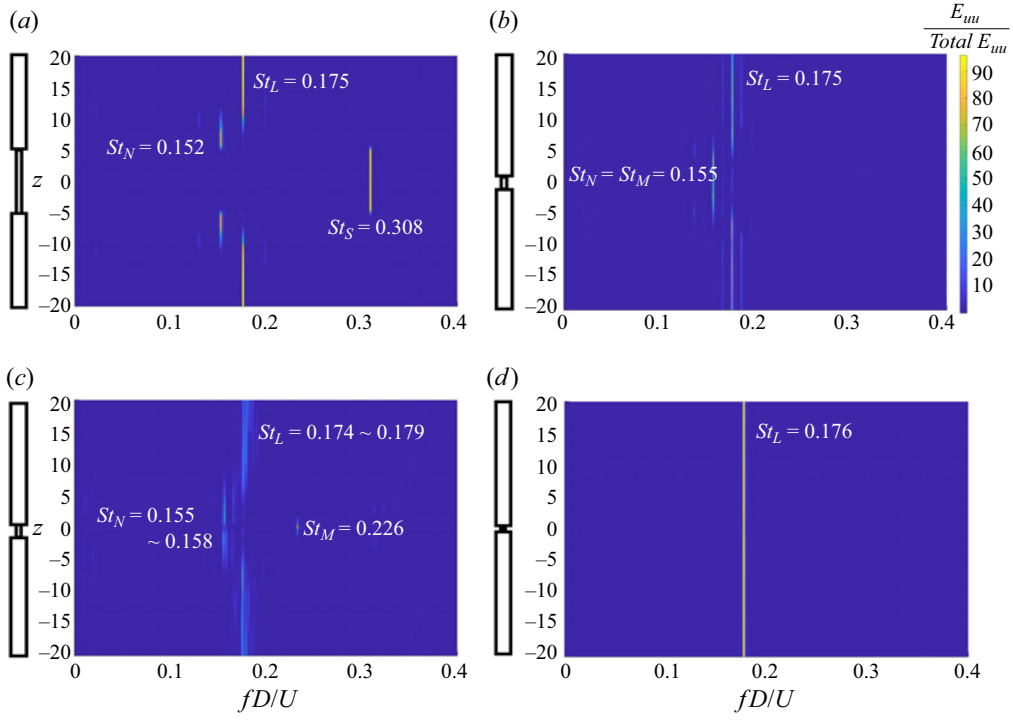

Figure 5. Streamwise velocity spectra are obtained from a fast Fourier transform (FFT) of time series of the streamwise velocity u along a vertical sampling line behind the I-shaped step cylinder at $(x, y) = (1.6, 0.4)$ over 1000 time unit (D/U) for (*a*) $l/D = 10$, (*b*) $l/D = 2.0$, (*c*) $l/D = 1.5$, (*d*) $l/D = 0.2$.

cells (the M-, N- and L-cell vortices) occur for the F3MNL mode (figure 4*c*), but with three dominant associated shedding frequencies (figure 5*c*) instead of the two observed for F2MNL. The fourth wake mode, denoted as the F1L mode, is found for $l/D = 0.2$. Here, one dominant vortex cell (the L-cell vortex) occurs (figure 4*d*) with only one dominant shedding frequency (figure 5*d*). Due to the different shedding frequencies of the dominant vortex cells for the first three wake modes (the F3SNL, F2MNL and F3MNL modes), the vortex dislocations occur between neighbouring vortex cells, where the NL-, NN- and LL-vortex loops (which were identified behind a single-step cylinder in Tian *et al.* 2020*b*) occur, as shown in figure 4(*a–c*). Figure 6 shows a periodic (in time) occurrence of the vortex dislocations visualized by the contours of the cross-flow velocity v along a spanwise sampling line at $(x, y) = (0.6, 0)$. The positive and negative values of v are due to the vortices shed from the $+Y$ and $-Y$ sides of the step cylinder, respectively. As l/D decreases, the similarity of the wake flow behind the single-step cylinder (as shown in figure 1*c*) and the I-shaped step cylinder (as shown in figure 4*a–d*) gradually disappears. The flow development and the formation mechanism of these four wake modes will be discussed in detail in the following sections.

3.1. *The F3SNL mode*

In the present section, the formation of the F3SNL mode will be discussed based on the $l/D = 10$ case. The mode F3SNL also occurs for $l/D = 5$ and 3; the corresponding wakes are shown in Appendix B. When the F3SNL mode occurs, the wake behind an

https://doi.org/10.1017/jfm.2024.1103 Published online by Cambridge University Press

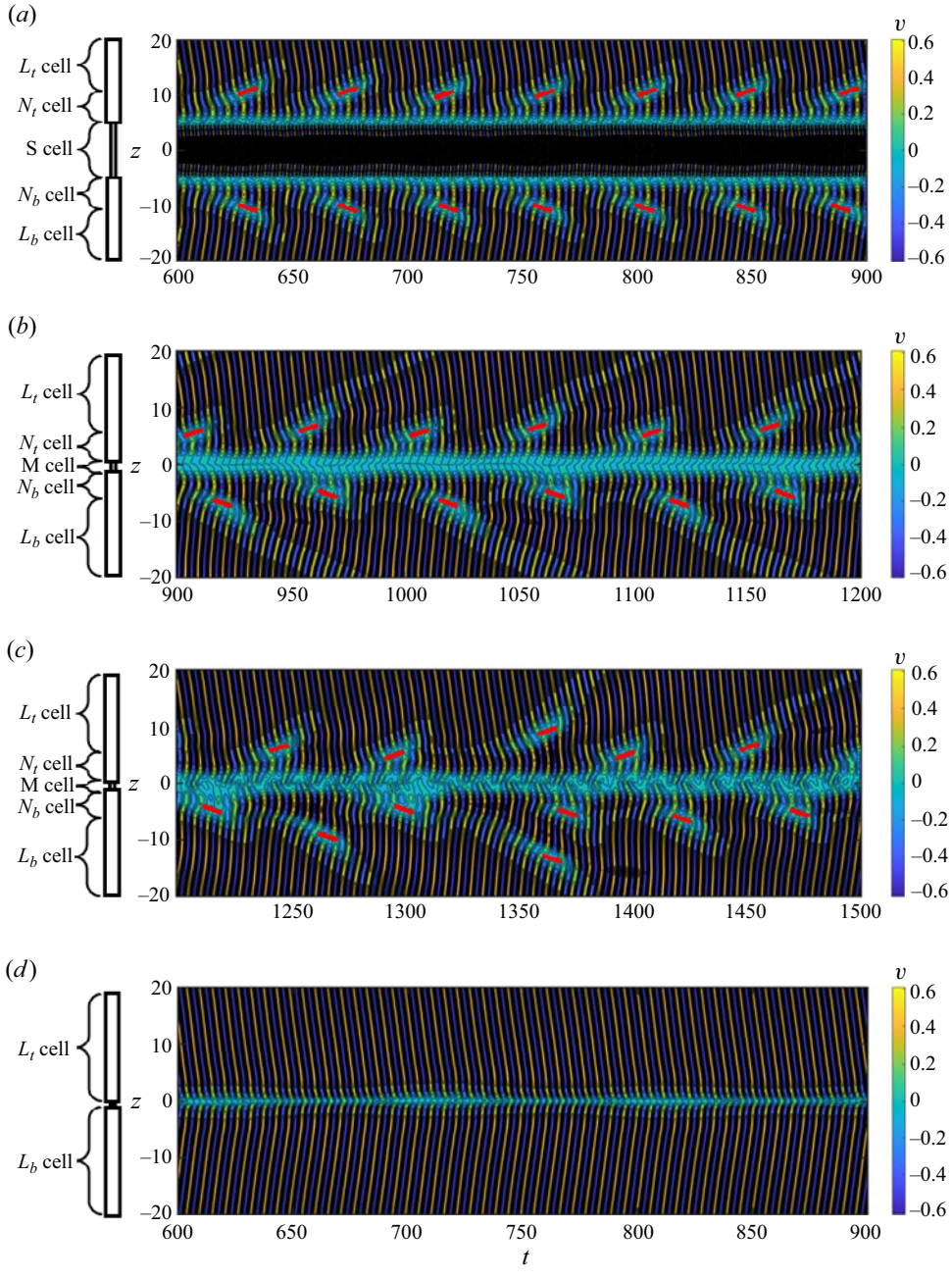

Figure 6. Cross-flow velocity component v as a function of the non-dimensional time, along the spanwise sampling line at $(x, y) = (0.6, 0)$ (*a*) for $l/D = 10$, (*b*) for $l/D = 2$, (*c*) for $l/D = 1.5$, (*d*) for $l/D = 0.2$. The red solid line indicates the vortex dislocations between the N- and L-cell vortices.

I-shaped step cylinder can be treated as a combination of two single-step cylinder wakes. Figure 4(*a*) shows that the three main spanwise vortices (S-, N- and L-cell vortices) which were originally identified by Dunn & Tavoularis (2006) behind the single-step cylinder (figure 1*c*) form in the wakes behind both the top part ($z > 0$) and the bottom part ($z < 0$)

https://doi.org/10.1017/jfm.2024.1103 Published online by Cambridge University Press

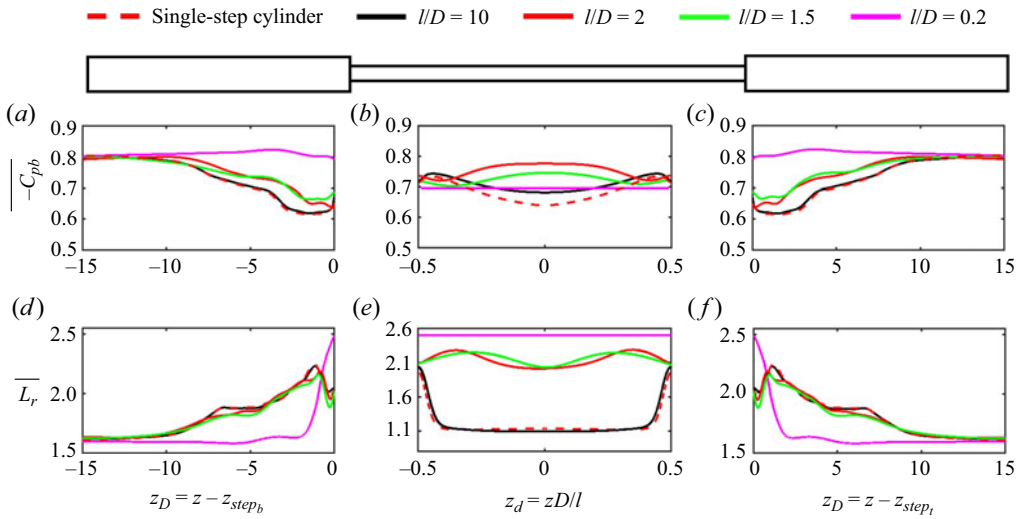

Figure 7. Distribution of time-averaged base pressure coefficient $\overline{C_{pb}}$ (*a*,*c*) on the large cylinder part and (*b*) on the small cylinder part. Distribution of recirculation length $\overline{L_r}$ (*d*,*f*) on the large cylinder part and (*e*) on the small cylinder part. The black, red, green and purple curves represent the corresponding distributions for $l/D = 10$, 2, 1.5 and 0.2. The red dashed curves represent the distributions along a single-step cylinder with $D/d = 2$ at $Re_D = 150$. The corresponding data are obtained from Tian *et al.* (2023). The horizontal axis for (*a*,*c*,*d*,*f*) is set as $z_D = z - z_{step}$ (where z_{step} represents the coordinate of the step on the corresponding part of the cylinder; subscripts b and t indicate the bottom and top parts of the I-shaped step cylinder), indicating the distance between the sampling position and the step. The horizontal axis for (*b*,*e*) is set as $z_d = zD/l$, indicating the relative sampling position on the small cylinder.

of the I-shaped step cylinder. Figure 5(*a*) shows that the S-cell vortex sheds behind the small cylinder with the largest shedding frequency St_S; the L-cell vortex sheds behind the large cylinder with the shedding frequency St_L; and the N-cell vortex sheds between the S- and L-cell vortices with the smallest shedding frequency St_N.

The formation of F3SNL is due to the length of the small cylinder (l) being so large that the interaction between the two steps can be neglected. The three-dimensional flow structures induced by each step are similar to those induced by the step of a single-step cylinder. Figure 7(*a*–*c*) shows the spanwise distribution of the time-averaged recirculation length L_r, which is obtained from the position where the time-averaged streamwise velocity crosses zero from negative to positive. Figure 7(*d*–*f*) shows the time-averaged base pressure coefficient $\overline{C_{pb}}$ along a spanwise sampling line located $0.02D$ downstream of the I-shaped step cylinder wall at $y = 0$. Here, $\overline{C_{pb}} = 2(\overline{p_b} - p_0)$, where $\overline{p_b}$ is the time-averaged base pressure and p_0 is the pressure at the outlet boundary. The distance $h = 0.02D$ is selected because it is slightly larger than the smallest cell's diagonal ($\sqrt{2}\Delta < h = 0.02D < 1.5\sqrt{2}\Delta$, where $\Delta = 0.01D$) such that we safely avoid wiggles possibly caused by cells directly cut by the cylinder surface and still stay as close as possible to the surface. It should be noted that the sampling line is located at different streamwise positions behind the small and large cylinders due to the different diameters of the small and large cylinders. As a reference, the distribution of $\overline{C_{pb}}$ and L_r along a single-step cylinder with $D/d = 2.0$ at $Re_D = 150$ is obtained in the region $-15 < z < 5$ from Tian *et al.* (2023) and plotted as the black dash line in figure 7(*a*–*f*). The comparison of $\overline{C_{pb}}$ and L_r between the $l/D = 10$ case (the red curve in figure 7) and the single-step cylinder (the red dashed curve in figure 7) shows tiny differences, with a maximum deviation of

https://doi.org/10.1017/jfm.2024.1103 Published online by Cambridge University Press

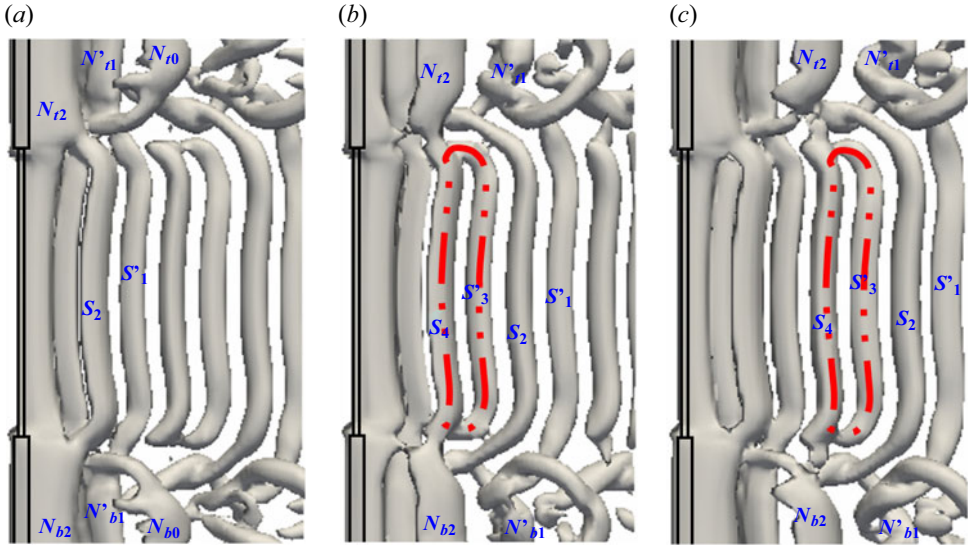

Figure 8. Isosurface of $\lambda_2 = -0.01$ in the region around the small cylinder for $l/D = 10$ showing developments of vortex structures on the $-Y$ side (*a*) at $t = 331.7$, (*b*) at $t = 335.4$, (*c*) at $t = 337.7$. The SS-loop is marked by the red dash-dot-dot line.

7 % appearing at $z_d = 1$ in figure 7(*d*). As a result, the formation of the S-, N- and L-cell vortices remains almost the same when the configuration changes from the single-step cylinder to the I-shaped step cylinder with $l/D = 10$.

Contrary to the single-step cylinder wake, where the S-N vortex dislocation occurs at the bottom of the small cylinder (figure 1*c*), the S-N vortex dislocation occurs at both the top and bottom of the small cylinder for $l/D = 10$ (as shown in figure 4*a*). This causes the topology of the S-S vortex loop to change from the half-loop for the single-step cylinder (reported by Dunn & Tavoularis (2006), Tian *et al.* (2017*a*) and visualized by the red dash-dot-dot curve in figure 1*c*) to the full loop for the I-shaped step cylinder (visualized by the red dash-dot-dot curve in figure 4*a*). The vortex interaction between the S- and N-cell vortices is further illustrated by consecutive snapshots of the isosurface of $\lambda_2 = -0.01$ in figure 8. All vortices are labelled by a combination of capital letters and numbers: 'N' and 'S' represent N- and S-cell vortices, respectively, while the number indicates the vortex shedding order. To differentiate between vortices shed from different sides of the cylinder, the capital letters with primes represent vortices shed from the $+Y$ side and pure capital letters represent vortices shed from $-Y$. When the S- and N-cell vortices just shed from the same cylinder side, they connect directly (e.g. S_2 connects directly to N_{t2} and N_{t2} in figure 8*a*). As they convect downstream, since the N-cell vortex contains a larger vortex strength than the S-cell vortex, all N-cell vortices split into at least two filaments (Morton & Yarusevych 2010). One connects to the subsequent N-cell vortex rotating in the opposite direction (e.g. a filament of N'_{b1} connects to N_{b2} from figure 8*a* to 8*b*); the other connects to the S-cell vortex rotating in the opposite direction (e.g. a filament of N'_{b1} connects to S_2 in figure 8*b*,*c*) or the same direction (e.g. a filament of N_{b2} connects to S_4 in figure 8*b*,*c*), depending on the phase alignment between the S- and N-cell vortices. The S-cell vortex that does not connect to any N-cell vortex connects to other S-cell vortices rotating in the opposite direction, forming the new SS-loop structure (e.g. S'_3 connects to S_4 in figure 8*b*,*c*).

https://doi.org/10.1017/jfm.2024.1103 Published online by Cambridge University Press

3.2. *The F2MNL mode*

In the present subsection, the formation of the F2MNL mode will be discussed based on the $l/D = 2$ case. This mode also occurs for $l/D = 2.5$, as shown in table 1; the wake for $l/D = 2.5$ is shown in Appendix B. As the wake mode changes from F3SNL to F2MNL, a comparison between figures 4(*a*) and 4(*b*) shows that the formation of the N- and L-cell vortices and the vortex dislocations between them are similar for $l/D = 10$ and $l/D = 2$, except that the S-cell vortex is absent for $l/D = 2$. Figure 5(*a*,*b*) further shows that, for $l/D = 10$ and $l/D = 2$, the shedding frequency of the N-cell vortex (St_N) and the L-cell vortex (St_L) does not change significantly (deviation <2 %), the frequency component St_S disappears and the frequency component St_N occurs both behind the small cylinder and behind the large cylinder close to the step ($-5 < z < 5$).

The formation of F2MNL is due to the fact that the decreasing length of the small cylinder (l) barely affects the flow characteristics behind the large cylinder, but significantly affects those behind the small cylinder due to the enhanced viscous suppression of the velocity fluctuations in the small cylinder near wake as the gap between the two steps decreases. Further details are discussed below. The comparison between the black and red solid curves in figure 7(*a*,*d*) shows that, as l/D decreases from 10 to 2, L_r and C_{pb} only slightly decrease along the large cylinder with no significant change in their distribution, and thus the formation of the N- and L-cell vortices are rarely affected. Along the small cylinder, the strong wake flow interactions between the two steps for $l/D = 2$ lead to a completely different distribution of L_r and C_{pb} compared with the $l/D = 10$ case. Even for the spanwise position $z_d = 0$ (i.e. $z = 0$) located in the middle of the small cylinder, which is least affected by the steps, L_r increases by around 95 % from $1.1D$ to $2.1D$ and $-C_{pb}$ increases by around 10 % from 0.7 to 0.78 when l/D decreases from 10 to 2. This is because the length of the small cylinder becomes too short to let the step effect decay along the small cylinder when l/D decreases from 10 to 2. For $l/D = 10$, the black solid curve in figure 7(*a–f*) shows that, due to the different diameters of the small and large cylinders, the base pressure ($-\overline{C_{pb}}$) is weaker and the recirculation length ($\overline{L_r}$) is smaller behind the small cylinder than behind the large cylinder away from the step (Rajani, Kandasamy & Majumdar 2009). However, the wakes behind the small and large cylinders mix, leading to a strengthened base pressure and increased recirculation length behind the small cylinder as the step is approached (referred to as the wake mixing effect). Unlike the $l/D = 10$ case, the short small cylinder length in the $l/D = 2$ case is not long enough for the wake mixing effect to vanish along the small cylinder. As a result, the red and black solid curves in figure 7(*b*,*e*) show that, in the vicinity of the step, $-\overline{C_{pb}}$ and $\overline{L_r}$ are similar for $l/D = 10$ and 2; as away from the step, $-\overline{C_{pb}}$ and $\overline{L_r}$ decreases for $l/D = 10$ but only exhibits a slight variation for $l/D = 2$. For $l/D = 2$, the recirculation length L_r remains larger than for $l/D = 10$ over the entire small cylinder, suppressing the instability in the near wake behind the small cylinder due to the increased viscous effects, leading to the disappearance of the S-cell vortex.

Figure 9(*a–f*) shows consecutive spanwise vorticity ($\omega_z = \partial v/\partial x - \partial u/\partial y$) contours in the xy-plane in the middle of the small cylinder ($z = 0$) for $l/D = 10$ (figure 9*a–c*) and for $l/D = 2$ (figure 9*d–f*). The time history of the lift coefficient (C_L) is shown in figure 9(*g*,*h*), where the time instants for figure 9(*a–f*) are marked. Here, $C_L = 2F_L(t)/\rho U^2 D_p L_c$, where F_L is the sampled lift force; $D_P = D$ for the large cylinder and $D_P = d$ for the small cylinder; L_c is the spanwise length of the part of the step cylinder where forces are sampled. Different from the staggered distribution of the vorticity ω_z behind the small cylinder for $l/D = 10$ shown in figure 9(*a–c*), figure 9(*d–f*) shows that ω_z is almost distributed

https://doi.org/10.1017/jfm.2024.1103 Published online by Cambridge University Press

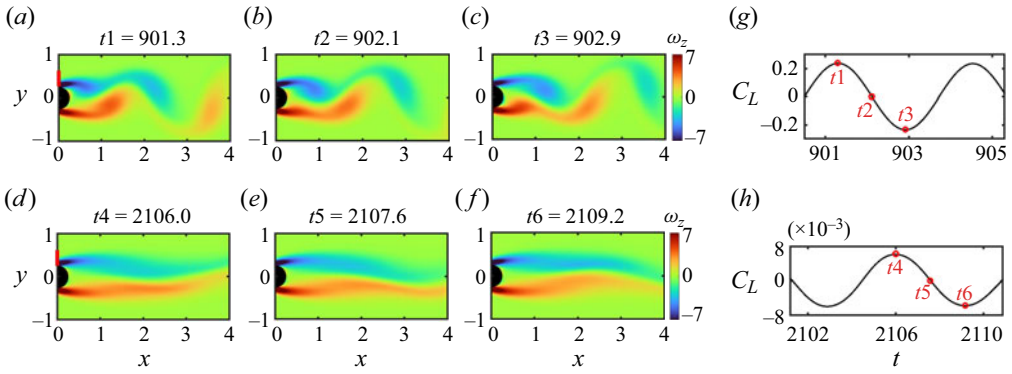

Figure 9. Consecutive instantaneous vorticity ω_z contours in the xy-plane at $z = 0$ showing the flow developments around the middle section of the cylinder: (a–c) for $l/D = 10$, (d–f) for $l/D = 2$. The corresponding time history of the lift coefficient for the centre part of the small cylinder at $z = 0$: (g) for $l/D = 10$ and (h) for $l/D = 2$.

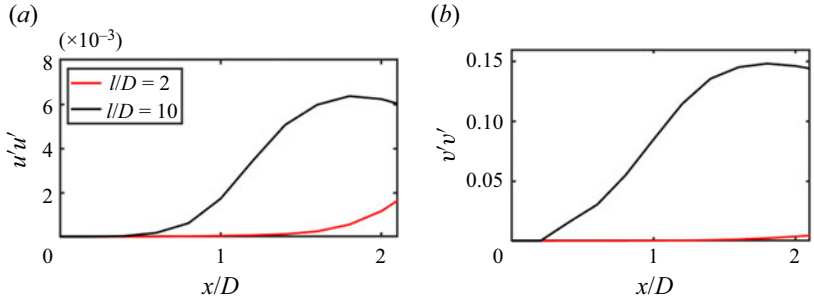

Figure 10. Distribution of velocity fluctuations along a horizontal sampling line at $(y, z) = (0, 0)$ (a) $u'u'$, (b) $v'v'$.

symmetrically on the $+Y$ and $-Y$ sides of the small cylinder in the near-wake region ($0.5 < z < 2$) for $l/D = 2$. This implies that no typical staggered Kármán vortices are shed behind the small cylinder for $l/D = 2$ (i.e. the vortex structures visualized by the isosurface of λ_2 behind the small cylinder in figure 4(b) are not the typical Kármán vortex). The underlying mechanism is that the shorter distance between the two steps for $l/D = 2$, compared with the $l/D = 10$ case, suppresses the velocity fluctuations in the near wake, leading to the absence of typical staggered Kármán vortex shedding behind the small cylinder.

Figure 10(a,b) shows the distribution of the velocity fluctuations along a streamwise sampling line at $(y, z) = (0, 0)$ for $l/D = 2$ (in red) and $l/D = 10$ (in black), indicating that the velocity fluctuations are highly suppressed for $l/D = 2$ compared with $l/D = 10$. In addition to stabilizing the near-wake fluctuations, the reduced distance between the two steps may also lead to a decrease in the upstream velocity of the small cylinder due to an enhanced frictional effect, causing the vorticity generation around the small cylinder to become insufficient for the S-cell formation. Whether the disappearance of the S-cell vortex is caused by the suppression of the vorticity generation around the small cylinder will be discussed below. The time-averaged circulation ($\Gamma = \int \int_A^B u|\omega| \, \mathrm{d}y \, \mathrm{d}t/T$, where $T = 100$ represents the integration time; the integration path (AB) is shown by the red solid line on the vertical axis in figure 9a,d) generated and convected into the wake

https://doi.org/10.1017/jfm.2024.1103 Published online by Cambridge University Press

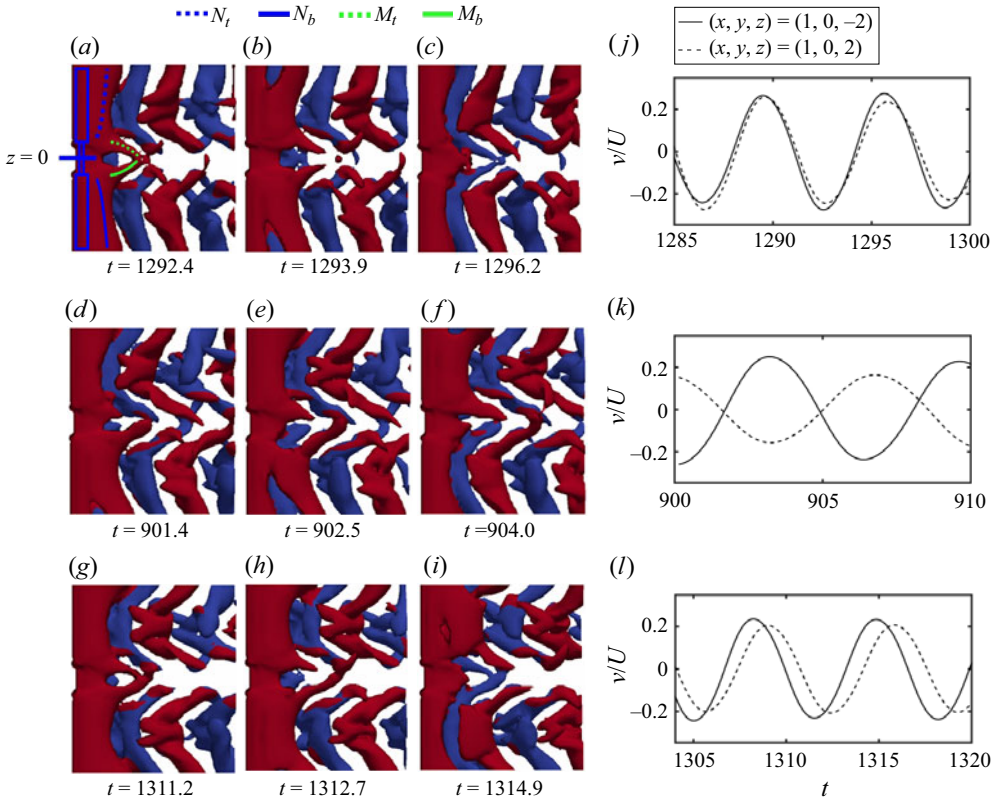

Figure 11. Isosurface of $\lambda_2 = -0.01$ in a close-up region around the small cylinder for $l/D = 2$ (indicated by the red rectangle in figure 4*b*) shows three types of M-cell vortex loops: (*a–c*) type 1 M-cell vortex loop, (*d–f*) type 2 M-cell vortex loop, (*g–i*) type 3 M-cell vortex loop. (*j–l*) Time history of the cross-flow velocity at $(x, y, z) = (1, 0, \pm 2)$ for type 1–3 M-cell vortex loops. The top (N_t) and bottom (N_b) N-cell vortices and the top (M_t) and bottom (M_b) parts of the M-cell vortices are indicated in (*a*). The blue and red colours indicate positive and negative spanwise vorticity, respectively.

from the small cylinder is estimated. The result shows that, from $l/D = 10$ to $l/D = 2$, Γ only decreases slightly (3 % from 1.25 to 1.22). Now, it is safe to conclude that, as the recirculation length sharply increases, the wake instability is highly suppressed for $l/D = 2$ compared with that for $l/D = 10$, leading to the disappearance of the S-cell vortex.

A further detailed investigation shows that, although only one dominant shedding frequency f_N is detected behind the small cylinder (figure 5*b*) for $l/D = 2$, the corresponding vortex structure is not the N-cell vortex. Figure 11(*a–e*) shows consecutive snapshots of the isosurface of $\lambda_2 = -0.01$ in a close-up region around the small cylinder for $l/D = 2.0$ (as marked by the red rectangle in figure 4*b*). It appears that a vortex-loop structure forms in the near wake behind the small cylinder (i.e. in the middle part of the I-shaped step cylinder). We identify this structure as the M-cell vortex loop due to the following two reasons: (*a*) although this vortex cell has the same shedding frequency as the N-cell vortex, it has a different topology. (*b*) The shape of the M-cell vortex for F2MNL is similar to the M-cell vortex for F3MNL; whereas the M-cell vortex in the F3MNL mode has a different shedding frequency and shape compared with the N-cell vortex, which will be discussed in detail in § 3.3. Figure 11 shows that all M-cell vortex loops in the F2MNL mode consist of at least a top part M-cell vortex (M_t) and a bottom part M-cell vortex (M_b),

https://doi.org/10.1017/jfm.2024.1103 Published online by Cambridge University Press

located at $z > 0$ and $z < 0$, respectively. Based on a long-time observation (approximately 300 shedding periods), three different types of M-cell vortex loops are observed: (type 1) the top and bottom parts of the M-cell vortex loop are from the same cross-flow side (either $+Y$ or $-Y$ side) of the cylinder (as shown in figure 11*a–c*); (type 2) the top and bottom parts of the M-cell vortex loop are from the opposite cross-flow side of the cylinder (as shown in figure 11*d–f*); (type 3) besides a pair of M_t and M_b from the same side of the cylinder, another M cell vortex from the opposite side of the cylinder also merges into the M-cell vortex loop (as shown in figure 11*g–i*).

For all three types of the M-cell vortex loops, figure 11 shows that complex vortex interactions occur as these M-cell loops form and convect downstream; however, no M-cell vortex is shed from (i.e. dislocates with) the corresponding N-cell vortex. In other words, all the M-cell vortices shed in phase with the corresponding N-cell vortices, thereby explaining why only one dominant frequency exists in the M- and N-cell regions ($-5 < z < 5$ in figure 5*b*). The different types of M-cell vortex loops result from variations in the phase relationship between N_t and N_b cells, which changes between in phase or out of phase. This phase difference can be measured by monitoring the time history of the cross-flow velocity (v) at $z_1 = 1$ in the N_t region and $z_2 = -1$ in the N_b region. When N_t and N_b shed in phase, e.g. from $t = 1292.4$ to $t = 1296.2$ (figure 11*a–c*), the time history of v at z_1 and z_2 peaks (with the same sign) almost simultaneously (figure 11*j*). Here, M_t and M_b form in phase at the same cross-flow side of the cylinder, inducing the type 1 M-loop. When N_t and N_b shed anti-phase, e.g. from $t = 901.4$ to $t = 904.0$ (figure 11*d–f*), the time history of v peaks with the opposite sign almost simultaneously (figure 11*k*). Here, M_t and M_b form in phase at the opposite cross-flow sides ($-Y$ and $+Y$ sides) of the cylinder, inducing the type 2 M-loop. When N_t and N_b shed partly out of phase (i.e. between in phase and anti-phase), the vortex strength between the corresponding N_t and N_b cells becomes unbalanced. To compensate for this, one more M-cell vortex on the weaker M-cell side joins the M-cell vortex loop (the type 3 M-loop). For example, M_b forms earlier than M_t in figure 11(*g*). This is also reflected by the velocity time history shown in figure 11(*l*): the black solid line (corresponding to N_t) shows an earlier peak than the black dashed line (corresponding to N_b). Therefore, during the formation of the corresponding M-loop, the strength of M_b is larger than M_t, causing the centre of the M-loop to move slightly in the $+z$ direction and merge with M_t.

3.3. *The F3MNL mode*

In the present subsection, the formation of the F3MNL mode will be discussed based on the $l/D = 1.5$ case. As shown in table 1, this mode also occurs for $l/D = 1$; the corresponding wake is shown in Appendix B. A comparison between figures 4(*b*) and 4(*c*) shows that both the F2MNL and F3MNL modes contain the M-, N- and L-cell vortices. Figure 5(*b*,*c*) further show two changes as l/D decreases from 2 to 1.5: (i) a new shedding frequency component St_M occurs in the small cylinder wake. This frequency is lower than the shedding frequency of the S-cell vortex for $l/D \geq 3$ and higher than the shedding frequency of the N- and L-cell vortices for all cases; (ii) the dominant shedding frequency behind the large cylinder becomes blurred. The underlying mechanisms will now be explained.

Although the M-cell vortex exists for both F2MNL and F3MNL, the occurrence of a new frequency component St_M in F3MNL is due to the fact that the M-cell vortex can dislocate from the corresponding N-cell vortex in F3MNL, making the M-cell vortex exhibit a different shedding frequency than the N-cell vortex. This is in contrast to the

https://doi.org/10.1017/jfm.2024.1103 Published online by Cambridge University Press

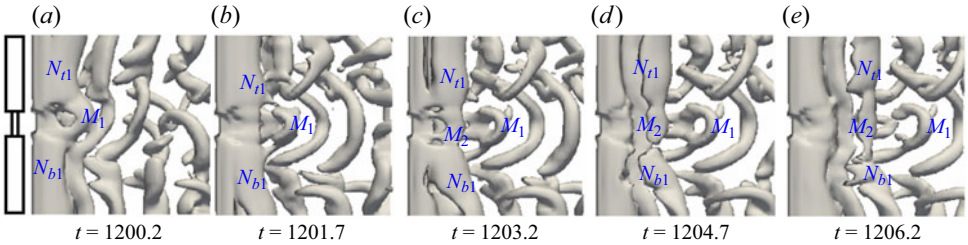

Figure 12. Isosurface of $\lambda_2 = -0.01$ in a close-up region around the small cylinder for $l/D = 1.5$ (indicated by the red rectangle in figure 4*c*) shows a vortex dislocation process when the M-cell vortex simultaneously dislocates from the corresponding top and bottom N-cell vortices.

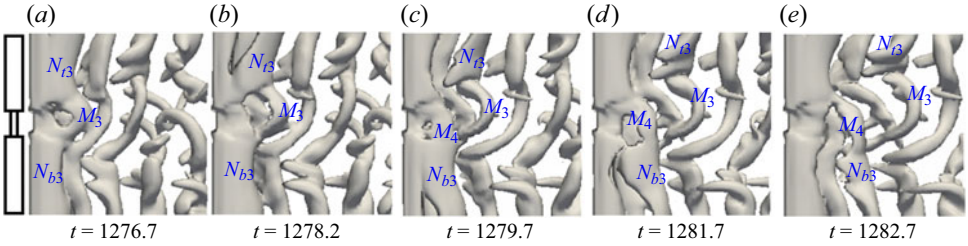

Figure 13. Isosurface of $\lambda_2 = -0.01$ in a close-up region around the small cylinder for $l/D = 1.5$ (indicated by the red rectangle in figure 4*c*) shows a vortex dislocation process when the M-cell vortex dislocates from the bottom N-cell vortex while it keeps the connection with the top N-cell vortex.

F2MNL mode, where the M-cell vortex always keep the one-to-one relationship with the N-cell vortex (as described in § 3.2). When dislocations occur between the M- and N-cell vortices, it appears that the M-cell vortex can either simultaneously dislocate from the top and bottom N-cell vortices or dislocate from only one of them, depending on the phase difference between the corresponding top and bottom N-cell vortices. Figure 12(*a–e*) shows consecutive snapshots of isosurfaces of $\lambda_2 = -0.01$ for $l/D = 1.5$ in the region around the small cylinder marked by the red rectangle in figure 4(*c*). At $t = 1200.2$, M_1 forms in figure 12(*a*). As M_1 convects downstream (figure 12*a–c*), it dislocates from the corresponding N-cell vortices N_{t1} and N_{b1}. Another M-cell vortex M_2 forms between N_{t1} and N_{b1} in figure 12(*d*,*e*). Here, the M-cell vortex M_1 simultaneously dislocates from the corresponding top (N_{t1}) and bottom (N_{b1}) N-cell vortices, because N_{t1} and N_{b1} almost shed in phase. When the top and bottom N-cell vortices are out of phase, the M-cell vortex can only dislocate from one of them. An example is shown in figure 13, where the M-cell vortex M_3 only dislocates from the bottom N-cell vortex N_{b3} but keeps connected with the top N-cell vortex N_{t3}. The dislocations between the M- and N-cell vortices persist in time. The contour of the cross-flow velocity v is plotted along a spanwise sampling line at $(x, y) = (0.6, 0)$ in figure 14. The positive and negative values of v, shown in the contours, are induced by the vortices shed from the $+Y$ and $-Y$ sides of the I-shaped cylinder, respectively. The number of M-cell vortices is larger than the number of N-cell vortices shed from $t = 1200$ to 1300, indicating a series of dislocations at the M-N boundary.

The two main reasons for the occurrence of the vortex dislocation between the M- and N-cell vortices when l/D decreases from 2 to 1.5 are (i) the larger vortex strength of the M-cell for $l/D = 1.5$ than for $l/D = 2$ and (ii) the higher convective velocity in the M-cell region than in the N-cell region. Firstly, as l/D decreases from 2 to 1.5, the decreased distance between the top and bottom N-cell vortices leads to more circulation energy

https://doi.org/10.1017/jfm.2024.1103 Published online by Cambridge University Press

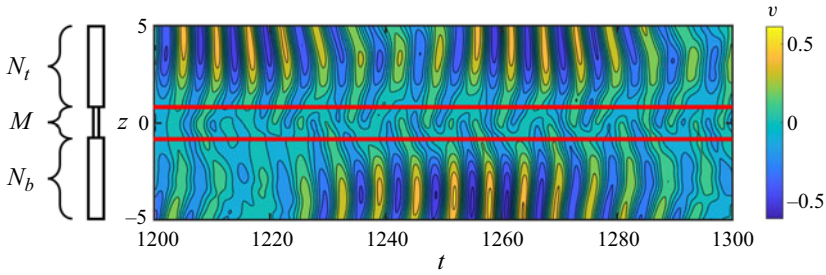

Figure 14. Cross-flow velocity component v as a function of the non-dimensional time, along the spanwise sampling line at $(x, y) = (0.6, 0)$ for $l/D = 1.5$.

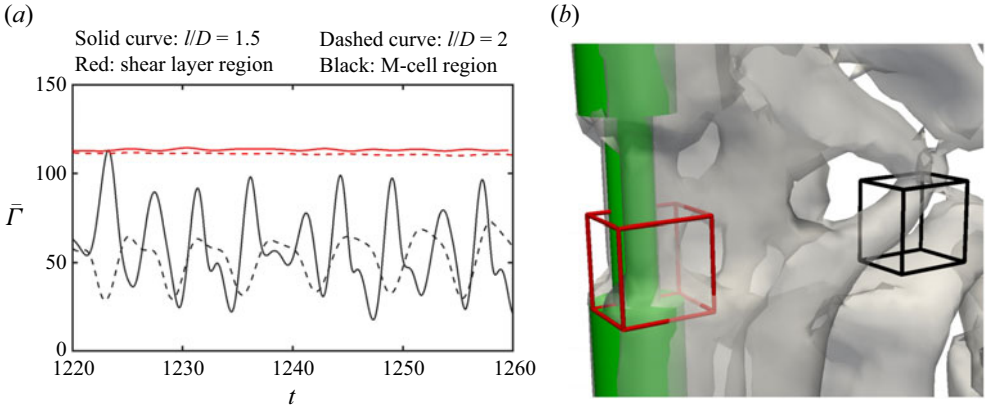

Figure 15. (*a*) Time history of the circulation strength in the M-cell region (solid black line for $l/D = 1.5$ and dashed black line for $l/D = 2$) and the shear layer around the small cylinder (solid red line for $l/D = 1.5$ and dashed red line for $l/D = 2$). (*b*) The red and black boxes show the flow volumes used to integrate the circulation strength in the shear layer around the small cylinder and the M-cell region, respectively.

being transferred from the N-cell region into the M-cell region, causing an increase in the circulation strength of the M-cell vortex. The total circulation strength (Γ) within a flow region in the present work is calculated based on $\Gamma_i = \sum_{j=1}^{N} |\omega_i| A_j$, where ω represents the vorticity, $i = x, y$ or z is the direction of ω, A represents the corresponding area perpendicular to the direction of ω and N is the total number of grid cells within the selected flow region. Then, the averaged circulation strength ($\bar{\Gamma}$) can be obtained by $\bar{\Gamma} = \sqrt{\Gamma_x^2 + \Gamma_y^2 + \Gamma_z^2}/VO$, where VO represents the volume of the selected flow region. Figure 15(*a*) shows the averaged circulation strength in the M-cell region (marked by the black box in figure 15*b*) and in the shear layer region of the small cylinder (marked by the red box in figure 15*b*) for $l/D = 2.0$ and 1.5. The black curves exhibit an oscillatory behaviour. Every time an M-cell vortex passes through the monitoring flow region, the black curves reach a peak. The red curve (shear region) remains almost unchanged since the corresponding monitoring flow region is located upstream of the position the M-cell vortex sheds. It appears that the circulation strengths within the shear layer around the small cylinder are comparable for $l/D = 2$ and 1.5. However, the circulation strength in the M-cell region increases substantially (i.e. the oscillation amplitude along the black solid curve for $l/D = 1.5$ is clearly higher than for the black dashed curve for $l/D = 2$).

https://doi.org/10.1017/jfm.2024.1103 Published online by Cambridge University Press

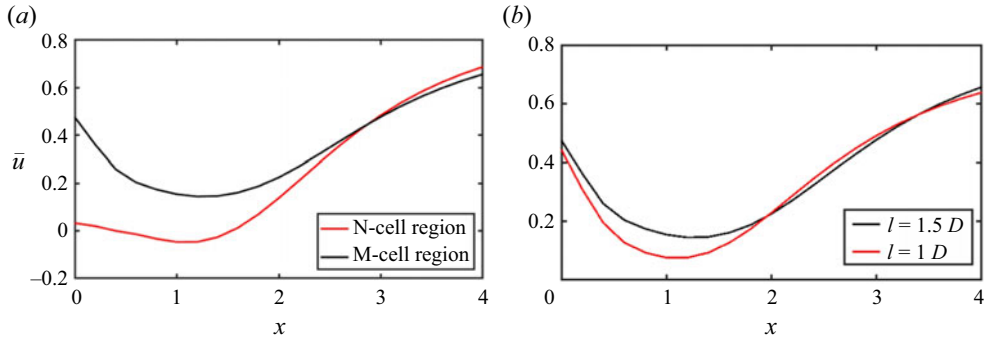

Figure 16. (*a*) Distributions of the mean streamwise velocity in the M-cell and N-cell regions for $l/D = 1.5$. (*b*) Distributions of the mean streamwise velocity in the M-cell region for $l/D = 1.5$ and 1.

These tendencies are due to more circulation energy being transferred from the N-cell region to the M-cell region as l/D decreases from 2 to 1.5. This stronger circulation strength makes the top and bottom parts of the M-cell vortex able to sustain themselves while disconnecting from the corresponding N-cell vortices as the M-cell vortex convects downstream for $l/D = 1.5$, instead of disconnecting from each other as for $l/D = 2$. Secondly, the smaller blockage effect of the small cylinder (compared with the large cylinder) causes the averaged convective velocity to become larger behind the small cylinder (the M-cell region) than behind the large cylinder (the N-cell region). Due to the spatial inhomogeneity of the convective velocity in the present case, it is difficult to evaluate an accurate convective velocity in the N- and M-cell regions. Yet, the mean streamwise velocity in the different vortex cell regions can be used to roughly compare the convective velocities in these regions. Figure 16 shows the averaged streamwise velocity in the M-cell region and the N-cell region, based on $\bar{u} = \sum_{j=1}^{N} u_j A_j / \sum_{j=1}^{N} A_j$, where N represents all grid cells within the sampling flow region, and A is the streamwise projection area of the corresponding grid cell. The flow region selected to calculate the averaged velocity is $-0.4 < y < 0.4$ (covering the concentrated swirling region in the wake behind the small cylinder with $D/d = 2$), $-l/2D < z < l/2D$ for the M-cell region and $-5 < z < 0$ for the N-cell region. Figure 16(*a*) indicates that the vortex in the M-cell region convects faster than that in the N-cell region. The higher convective velocity and stronger circulation strength cause the new shedding frequency of the M-cell vortex, St_M, to occur for $l/D = 1.5$. Our explanation can be further confirmed by checking the variation of the shedding frequency of the M-cell vortex when l/D decreases from 1.5 to 1.0. The corresponding mean streamwise velocity distribution and shedding frequencies are shown in figures 16(*b*) and 31(*b*) (Appendix B), indicating that, as the convective velocity behind the small cylinder decreases, the shedding frequency of the M-cell vortex decreases from 0.23 for $l/D = 1.5$ to 0.21 for $l/D = 1$.

Another interesting phenomenon for the F3MNL mode is that the frequency contours become blurred behind the large cylinder in the N- and L-cell vortex regions, as shown in figure 5(*c*). This is caused by the interactions between the M- and N-cell vortices described above. Figure 17(*a*,*b*) compares the time history of the downwash flow (spanwise flow) and the base pressure in the vicinity of the step behind the large cylinder for $l/D = 2$, $l/D = 1.5$ and $l/D = 0.2$. As pointed out by Tian *et al.* (2020*a*), the formation mechanism of the N-cell vortex is closely related to the step-induced variations of the spanwise velocity (w) and the base pressure. As l/D decreases from 2.0 to 1.5, the occurrence of the vortex

https://doi.org/10.1017/jfm.2024.1103 Published online by Cambridge University Press

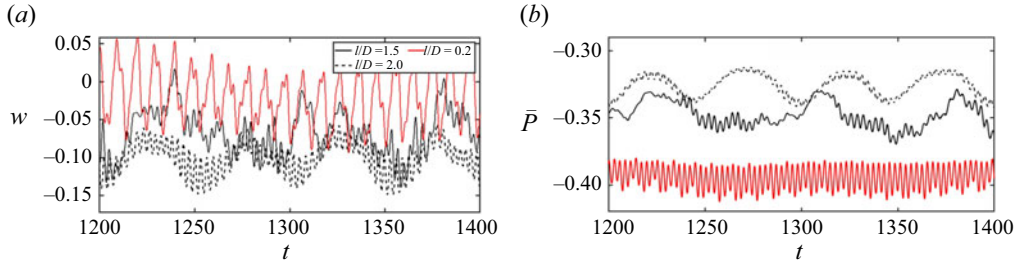

Figure 17. (*a*) Time history of the spanwise velocity w at $(x, y, z_D) = (0.6, 0, -0.1)$, where z_D is defined in figure 7 for $l/D = 2.0$, 1.5 and 0.2. (*b*) Time history of the base pressure at $(x, y, z_D) = (0.51, 0, -0.1)$. The period of the vortex dislocation between the N- and L-cell vortices for $l/D = 2.0$ is marked.

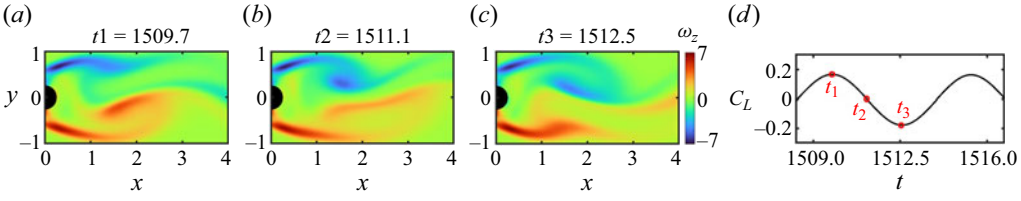

Figure 18. (*a–c*) Consecutive instantaneous vorticity ω_z contours in the xy-plane at $z = 0$ showing the flow developments around the middle section of the cylinder for $l/D = 0.2$. (*d*) The corresponding time history of the lift coefficient for the centre part of the small cylinder at $z = 0$.

dislocation between the M- and N-cell vortices disturbs the wake flow and induces a more irregular and sharp variation of the spanwise velocity and the base pressure for $l/D = 1.5$ (the black solid line in figure 17*a*,*b*) than for $l/D = 2.0$ (the black dashed line in figure 17*a*,*b*). This causes the shedding frequencies of the N- and L-cell vortices to be unstable for $l/D = 1.5$, leading to a blurred frequency contour behind the large cylinder for $l/D = 1.5$, as shown in figure 5(*c*). Another consequence of the unstable shedding frequencies (St_N and St_L) is that the regularity of the vortex dislocations between the N- and L-cell vortices becomes weaker for $l/D = 1.5$ than for $l/D = 10$ and 2. As shown in figure 6(*a–c*), the formation position and the period of the NL-dislocation vary only for $l/D = 1.5$.

3.4. *The F1L mode*

In the present section, the formation of the F1L mode will be discussed based on the $l/D = 0.2$ case. A comparison between figures 4(*c*) and 4(*d*) shows two differences as the flow changes from the F3MNL to the F1L mode: (i) the N- and M-cell vortices disappear, while the L-cell vortex becomes the only dominant vortex; (ii) the streamwise vortices form regularly between the L-cell vortices shed from the different sides of the I-shaped step cylinder.

To be certain that the vortex in the small cylinder wake belongs to the L-cell vortex instead of the M-cell vortex, figure 18(*a–c*) shows consecutive spanwise vorticity ω_z contours in the xy-plane in the middle of the small cylinder ($z = 0$) for $l/D = 0.2$. The corresponding time history of C_L is shown in figure 18(*d*). It appears that the vortices behind the small cylinder are generated from the shear layer located at $y = \pm 0.5$ (figure 18*a–c*). Since $y = \pm 0.5$ is located at the surface of the large cylinder, the vortices behind the small cylinder are mainly from the shear layer of the large cylinder, belonging to the L-cell vortex. The disappearance of the M-cell vortex as l/D decreases from 2 to 0.2

https://doi.org/10.1017/jfm.2024.1103 Published online by Cambridge University Press

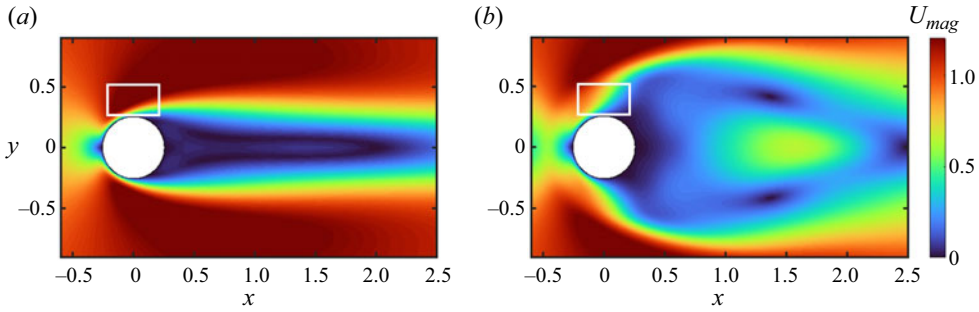

Figure 19. Time-averaged magnitude of the velocity ($U_{mag} = \sqrt{u^2 + v^2 + w^2}$) on the xy-plane in the middle of the small cylinder ($z = 0$): (a) for $l/D = 2$, (b) for $l/D = 0.2$.

is caused by the fact that the shorter distance between the two steps highly suppresses the surrounding velocity around the small cylinder, thus suppressing the generation of circulation. Figure 19 shows the contours of the time-averaged velocity magnitude ($U_{mag} = \sqrt{u^2 + v^2 + w^2}$) on the xy-plane in the middle of the small cylinder for $l/D = 2$ and 0.2. It shows that the surrounding flow around the small cylinder (e.g. the region encircled by the white rectangle in figure 19) in the $l/D = 0.2$ case is clearly weaker than that in the $l/D = 2$ case. As a result, the circulation generated from the $+Y$ and $-Y$ sides of the small cylinder is clearly smaller for $l/D = 0.2$ (as shown in figure 18a–c) than for $l/D = 2$ (as shown in figure 9e–g), leading to the disappearance of the M-cell vortex.

The vanishing of the N-cell vortex is due to the fact that the three-dimensional effect of the step on the large cylinder wake becomes weak as the length of the small cylinder decreases to $0.2D$. Figure 17(a,b) shows that the fluctuation of the downwash flow and the base pressure become much more regular and weaker for $l/D = 0.2$ than for $l/D = 1.5$ and 2.0; and these two flow quantities dominate the formation of the N-cell vortex (Tian *et al.* 2020a). The formation of the regular streamwise vortices between the neighbouring L-cell vortices is due to the step disturbing the wake. Firstly, the spanwise velocity (w shown in figure 17a) triggered by the step contributes to the formation of the streamwise vorticity ($\omega_x = \partial w/\partial y - \partial v/\partial z$). Secondly, the above-mentioned velocity suppression effect of the two steps, and the small diameter of the small cylinder, cause the circulation strength of the L-cell vortex to be smaller behind the small cylinder than behind the large cylinder away from the step. This is illustrated by the time history of the circulation strength (Γ) within the flow volume just behind the small cylinder (marked by the red box in figure 20b) and behind the large cylinder away from the step (marked by the black box in figure 20b). Only the L-cell vortices shed from the $-Y$ side of the cylinder are monitored. This difference in vortex strength induces part of the L-cell vortex to split and connect to the other L-cell vortices, which shed from the opposite side of the cylinder, as shown in figure 4(d).

4. The streamwise vortex system around the I-shaped step cylinder

The streamwise vortex system around the single-step cylinder was initially investigated by Dunn & Tavoularis (2006), where a pair of edge vortices and a junction vortex were identified. The junction vortex forms on the joint surface between the small and large cylinders (i.e. on the step surface), upstream of the small cylinder; the edge vortex originates from the edge of the step surface. These vortices are sketched in figure 21.

https://doi.org/10.1017/jfm.2024.1103 Published online by Cambridge University Press

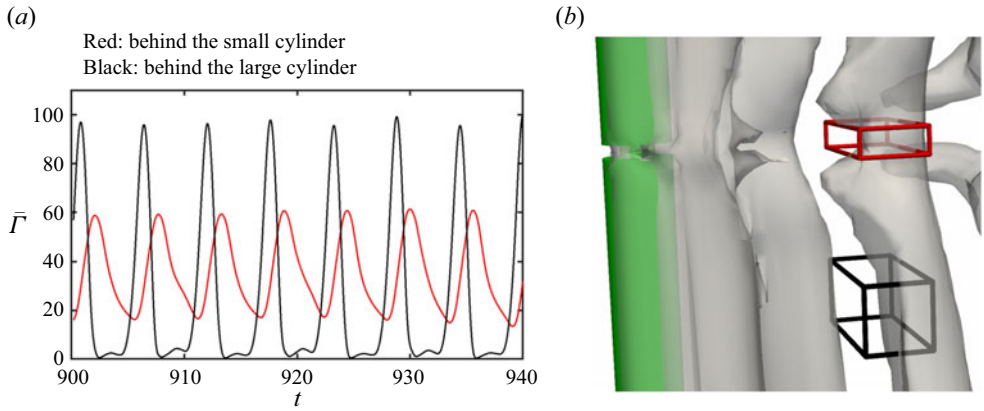

Figure 20. (*a*) Time history of the circulation strength in the wake behind the small and large cylinders for $l/D = 0.2$. (*b*) The red box ($3 < x < 4$, $-1 < y < 0$ and $-0.1 < z < 0.1$) and black box ($3 < x < 4$, $-1 < y < 0$ and $-3 < z < 2$) show the flow volumes used to calculate the circulation strength behind the small and large cylinders, respectively.

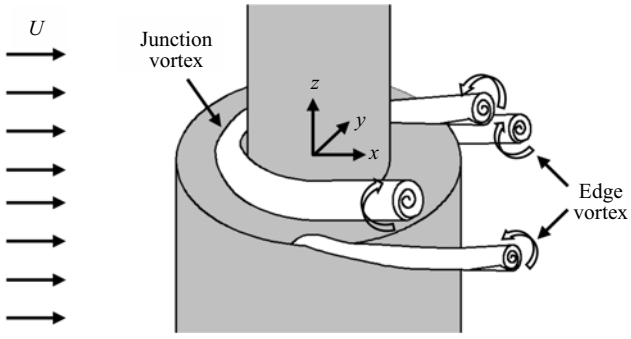

Figure 21. Sketch of the streamwise vortices forming around a step cylinder, reproduced based on figure 2 in Dunn & Tavoularis (2006).

The purpose of this section is to show how the distance between the two steps affects the streamwise vortex system around the I-shaped dual-step cylinder.

Firstly, the formation of the streamwise vortex system is investigated based on the time-averaged flow field. Since the time-averaged flow fields shown in figure 7(*a–f*) are symmetric about the middle of the step cylinder for all wake modes, the discussion in the present section is concerned only with the bottom half of the I-shaped cylinder, i.e. $z < 0$. Figure 22 shows isosurfaces of the time-averaged $\lambda_2 = -2$ and the isosurface of the streamwise vorticity $\omega_x = \pm 1$ around the bottom part of the I-shaped step cylinder. As in figure 4, results are presented only for the four different configurations $l/D = 10$, 2, 1.5 and 0.2, each representing one of the four characteristic wake modes described in §§ 3.1–3.4. It appears that a pair of edge vortices and a junction vortex form around the I-shaped step cylinder for the F3SNL, F2MNL and F3MNL modes. The edge vortices and junction vortices rotate in opposite directions on the same side of the step surface, similar to the single-step cylinder case depicted in figure 21. Figure 22(*d*,*h*) shows that, for the F1L mode ($l/D = 0.2$), the junction vortex disappears and only a pair of edge vortices exist. This is because the gap $l/D = 0.2$ between the two steps is too narrow for the formation of

https://doi.org/10.1017/jfm.2024.1103 Published online by Cambridge University Press

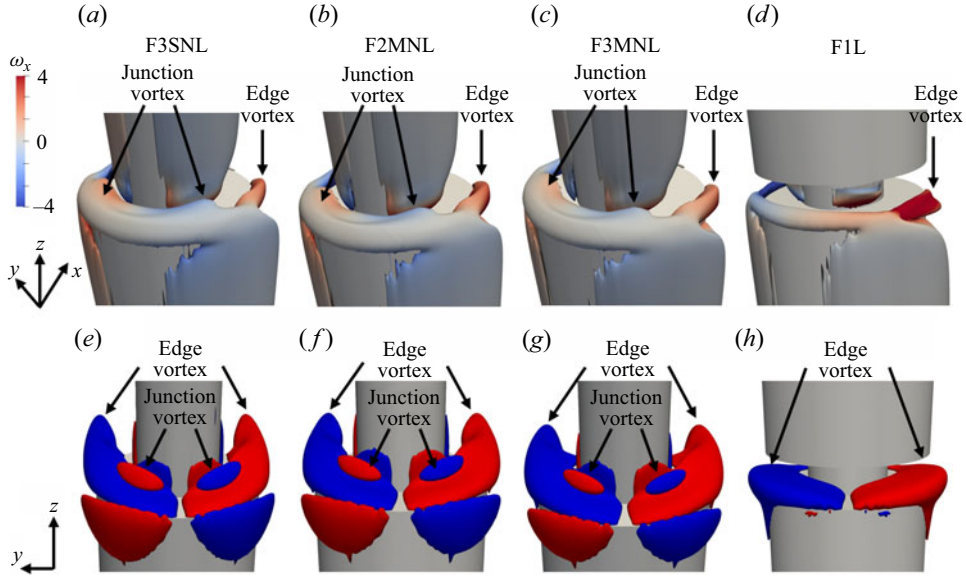

Figure 22. Isosurface of the time-averaged $\lambda_2 = -2$ coloured by the streamwise vorticity for (*a*) $l/D = 10$, (*b*) $l/D = 2$, (*c*) $l/D = 1.5$, (*d*) $l/D = 0.2$. Isosurface of the time-averaged streamwise vorticity $\omega_x = 1$ in red and $\omega_x = -1$ in blue for (*e*) $l/D = 10$, (*f*) $l/D = 2$, (*g*) $l/D = 1.5$, (*h*) $l/D = 0.2$.

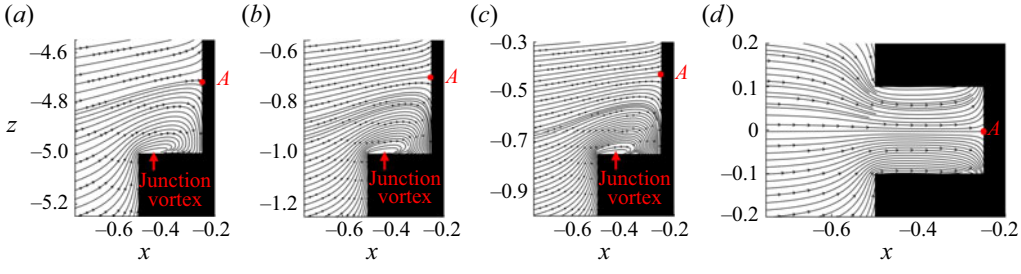

Figure 23. Time-averaged streamlines on the *xz*-plane at $y = 0$ for (*a*) $l/D = 10$, (*b*) $l/D = 2$, (*c*) $l/D = 1.5$ and (*d*) $l/D = 0.2$. The junction vortex and the impinging attachment point (point A) are marked.

the junction vortex. This is further visualized in figure 23(*a–c*), showing the time-averaged streamlines in the centre plane ($y = 0$) just in front of the step for $l/D = 10$, 2 and 1.5. When the distance between the two steps is large enough, the junction vortex is caused by both the flow separation at the leading edge of the step and the impingement of the flow at the surface of the small cylinder. After the flow separates at the leading edge of the step, it impinges on the upstream surface of the small cylinder at the attachment point A (see figure 23*a–c*), where a part of the flow deflects downward and recirculates into the junction vortex. However, when the gap between the two steps becomes too short, there is not enough space for this downward flow to recirculate into the junction vortex. Figure 23(*d*) shows that the flow almost aligns in the streamwise direction above the step surface for $l/D = 0.2$.

The formation of the edge vortices around the I-shaped step cylinder is similar to that around the single-step cylinder, where the flow is pushed sideways due to the blockage of

https://doi.org/10.1017/jfm.2024.1103 Published online by Cambridge University Press

the small cylinder, spilling over the edges of the step surface and rolling up into the edge vortex (Dunn & Tavoularis 2006). The instantaneous dynamics of the streamwise vortex system is not investigated here because it was found that, in the present laminar Reynolds number regime, the streamwise vortices are almost stable around the step surface. For example, the fluctuations of the circulation strength in the region containing the junction and edge vortices are negligible, as shown by the red curves in figure 15(*a*).

Overall, except for the case where the gap between the two steps becomes too small (e.g. $l/D = 0.2$), the streamwise vortex system around the I-shaped step cylinder is similar to that around the single-step cylinder where a pair of edge vortices and a junction vortex occur. In the exceptional $l/D = 0.2$ case, the junction vortex disappears.

5. Structural loads on I-shaped step cylinders

For cylindrical structures, the time-averaged drag force and the root-mean-square of the lift force are usually investigated to quantify the overall steady and unsteady forces acting on the structure, which are essential for assessing resistance and potential for vibration-induced fatigue. The structural load distribution along single-step cylinders was described in Tian *et al.* (2023): along the large cylinder, due to step effects and the pressure difference between the small and the large cylinder wakes, the mean drag coefficient decreases towards the step until it reaches a minimum (see figure 24*a*); then, it increases towards the step. The root mean square value of the lift coefficient decreases towards the step because of the distortion of vortices near the step. During this decrease, a minimum (see figure 24*c*) occurs due to the vortex dislocations between the N- and L-cell vortices; the effect of these vortex dislocations on the structural load was discussed in detail in Tian *et al.* (2023). Along the small cylinder, both the time-averaged drag coefficient and the root mean square value of the lift coefficient decrease towards the step (see figure 24*b*,*d*) since the velocity is suppressed by the step surface and the vortices are distorted around the step.

As the configuration changes from a single-step cylinder to an I-shaped dual-step cylinder, the interactions between the two steps become severe as the gap between the steps decreases. This gives rise to two research questions: (i) How are the structural loads distributed along the I-shaped dual-step cylinder as the gap between the steps varies? (ii) And how do the different wake modes affect these distributions? These are discussed in detail below. As in § 3, results are presented only for the four different configurations $l/D = 10$, 2, 1.5 and 0.2, each of which is representative of one of the four characteristic wake modes described in §§ 3.1–3.4. The definitions of the time-averaged drag coefficient $\overline{C_D}$ and the root-mean-square of the lift coefficient $\overline{C_L'}$ are

$$\overline{C_D} = \frac{1}{N}\sum_{i=1}^{N}\frac{2F_{D,i}(t)}{\rho U^2 D_p L_c} \tag{5.1}$$

$$\overline{C_L'} = \sqrt{\frac{1}{N}\sum_{i=1}^{N}(C_{L,i} - \overline{C_L})^2}, \quad C_L = \frac{2F_L(t)}{\rho U^2 D_p L_c}, \quad \overline{C_L} = \frac{1}{N}\sum_{i=1}^{N} C_{L,i}, \tag{5.2a–c}$$

where N is the number of values in the sample, and $F_D(t)$ and $F_L(t)$ are the instantaneous drag (the structural load in the x-direction) and lift (the structural load in the y-direction) forces acting on the structure, respectively. Here, C_L and $\overline{C_L}$ are the instantaneous and time-averaged lift force coefficients; $D_p = D$ for the large cylinder and $D_p = d$ for the

https://doi.org/10.1017/jfm.2024.1103 Published online by Cambridge University Press

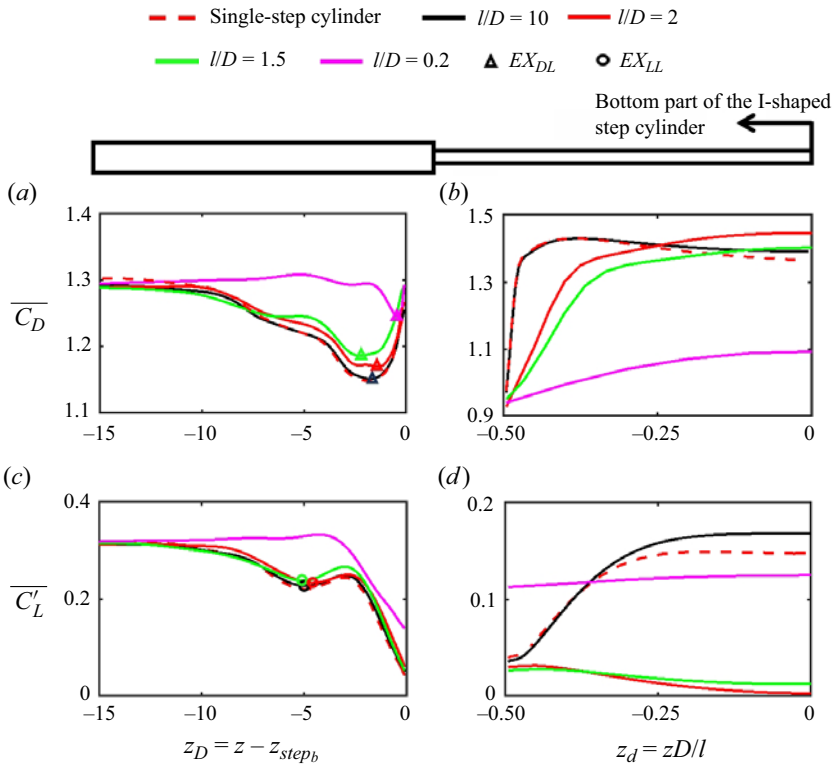

Figure 24. The distributions of structural loads in the $l/D = 10$, 2, 1.5 and 0.2 cases are plotted in black, red, green and purple, respectively. The spanwise distribution of the total drag coefficient $\overline{C_D}$ (*a*) along the large cylinder; (*b*) along the small cylinder. The spanwise distribution of the root mean square of lift coefficient $\overline{C_L'}$ (*c*) along the large cylinder; (*d*) along the small cylinder. The local minima of $\overline{C_D}$ and $\overline{C_D}$ along the large cylinder are indicated by the triangle and circle. In (*a*,*c*), the local extremes of the drag coefficient EX_{DL} and the lift coefficient EX_{LL} are marked in all cases.

small cylinder; $L_c = 0.05D$ is the spanwise length of the step cylinder for which forces are calculated.

5.1. *Structural load along the large cylinder*

Figure 24(*a*,*c*) shows the distributions of $\overline{C_D}$ and $\overline{C_L'}$ along the large cylinder, while figure 24(*b*,*d*) shows the distributions of $\overline{C_D}$ and $\overline{C_L'}$ along the small cylinder; the structural load distribution along a single-step cylinder with $D/d = 2$ for $Re_D = 150$ (adopted from Tian *et al.* 2023) is given for comparison. As l/D decreases from 10 to 1.5, figure 24(*a*,*c*) shows that the distributions of $\overline{C_D}$ and $\overline{C_L'}$ along the large cylinder are qualitatively similar to those for the single-step cylinder. This is because the dominant vortex cells (the N- and L-cell vortices) are similar for the F3SNL, F2MNL and F3MNL modes, as well as for the single-step cylinder (see figures 1*c* and 4*a*–*c*). In figure 24(*a*,*c*), the local extremes of drag coefficient EX_{DL} and lift coefficient EX_{LL} are marked by triangles and circles, respectively, for all cases.

As l/D decreases to 0.2, an apparent change of $\overline{C_L'}$ is the disappearance of the local minimum EX_{LL} (see figure 24*a*). The occurrence of this minimum for $l/D = 10$, 2 and

https://doi.org/10.1017/jfm.2024.1103 Published online by Cambridge University Press

Wake mode	F3SNL		F2MNL		F3MNL		F1L	
l/D	10		2		1.5		0.2	
z	−6.7	−5.1	−2.3	−1.1	−2.95	−0.85	−0.5	−0.2
$\overline{C_{Dp}}$ (fore part)	0.24	0.26	0.23	0.25	0.23	0.25	0.25	0.31
$\overline{C_{Dp}}$ (aft part)	0.68	0.74	0.71	0.76	0.72	0.77	0.76	0.74
Total $\overline{C_{Dp}}$	0.92	1.00	0.94	1.01	0.95	1.02	1.01	1.05
Total $\overline{C_D}$	1.15	1.24	1.17	1.26	1.19	1.28	1.24	1.29
R	89 %		78 %		78 %		80 %	

Table 2. Time-averaged pressure-induced drag force coefficient ($\overline{C_{Dp}}$) and total drag force coefficient ($\overline{C_D}$) on the fore part ($x < 0$) and the aft part ($x > 0$) of the cylinder for different wake modes at EX_{DL} and the position $0.1D$ away from the step surface. The shaded columns represent the position $0.1D$ away from the step. From EX_{DL} to the position $0.1D$ below the step, the ratio of the change in total $\overline{C_D}$ due to pressure is shown in the last line, $R = \Delta\overline{C_{Dp}}/\Delta\overline{C_D}$.

1.5 is caused by the vortex dislocations between the N- and L-cell vortices: Tian *et al.* (2023) reported that the formation of such vortex dislocations can cause a 90 % reduction in the local lift amplitude. The series of vortex dislocations at the N-L cell boundary for $l/D = 10$, 2 and 1.5 shown in figures 4(*a–c*) and 6(*a–c*), are underpinning the local minima EX_{LL}. As the vortex dislocations between the N- and L-cell vortices disappear for $l/D = 0.2$ due to the absence of the N-cell vortex (see figure 6*d*), the local minimum EX_{LL} also disappears. As a result, $\overline{C_L'}$ becomes larger along the small cylinder for $l/D = 0.2$ than for $1.5 < l/D < 10$.

For all the cases, $\overline{C_D}$ decreases towards the step along the large cylinder until reaching the local minimum EX_{DL}, and then increases towards to the step. This is similar to the behaviour observed for the single-step cylinder (Tian *et al.* 2023). However, a detailed investigation reveals that the mechanism underpinning the increase of $\overline{C_D}$ from EX_{DL} towards the step is different for the $l/D = 0.2$ case than for the other cases.

This is further detailed in table 2, showing the total drag coefficient $\overline{C_D}$, and the pressure-induced drag coefficient over the fore part and aft part of the cylinder, as well as over the entire cylinder at EX_{DL} and at $z_D/D = -0.1$ (i.e. $0.1D$ away from the step). The ratio of the change in $\overline{C_D}$ due to the pressure is also given as $R = \Delta\overline{C_{Dp}}/\Delta\overline{C_D}$. Firstly, R is larger than 78 % for all cases, indicating that the pressure-induced drag coefficient $\overline{C_{Dp}}$ dominates the variation of the total drag coefficient. Secondly, the increase of the pressure-induced drag coefficient $\overline{C_{Dp}}$ is mainly due to the increased $\overline{C_{Dp}}$ on the aft part of the cylinder for the F3SNL, F2MNL and F3MNL modes. This is similar to the mechanism reported for the single-step cylinder (Tian *et al.* 2023). However, for the F1L mode, the increase of pressure-induced drag coefficient $\overline{C_{Dp}}$ is caused by the increased $\overline{C_{Dp}}$ on the fore part of the cylinder; the pressure-induced drag coefficient on the aft part of the cylinder decreases slightly from EX_{DL} to the step for the F1L mode, as opposed to the other modes. These different behaviours between the F3SNL, F2MNL and F3MNL modes on one side, and the F1L mode on the other side, are due to the different wake modes around the I-shaped step cylinders. For the F3SNL, F2MNL and F3MNL modes, there are three vortex cells behind the I-shaped step cylinder. Figure 7(*d*) shows that the recirculation length in the N-cell vortex region is larger than in the neighbouring L-cell and S-cell (or M-cell) vortex regions, leading to a non-monotonic variation of the recirculation

https://doi.org/10.1017/jfm.2024.1103 Published online by Cambridge University Press

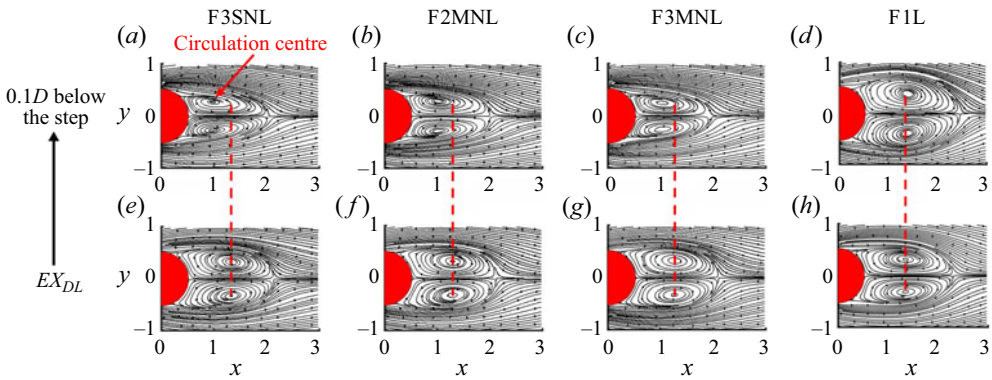

Figure 25. Time-averaged streamlines on xy-planes behind the large cylinder: (a–d) at $z_D = -0.1$ for $l/D =$ 10, 2, 1.5 and 0.2; (e–h) at the local minimum point EX_{DL} shown in figure 24(a) for $l/D = 10$, 2, 1.5 and 0.2. The red reference line indicates the location of the circulation centre on the xy-plane.

length along the large cylinder. The time-averaged streamlines in the xy-planes reveal that the circulation centre moves upstream as the step is approached, thus strengthening the pressure behind the large cylinder, leading to an enhanced pressure force on the aft part of the cylinder for the F3SNL, F2MNL and F3MNL modes (see table 2). For the F1L mode, however, the L-cell vortex is the only dominant vortex cell behind the step cylinder, leading to a monotonic variation of the recirculation length along the large cylinder, as shown in figure 7(d). Figure 25(d,g) shows that the recirculation centre moves slightly downstream as the step is approached, thereby weakening the pressure behind the large cylinder, thus leading to the slightly decreased pressure force on the aft part of the cylinder (see table 2).

5.2. *Structural load along the small cylinder*

As the configuration changes from the single-step cylinder to the I-shaped dual-step cylinder with different gaps between the two steps, the structural load is more affected along the small cylinder than along the large cylinder. First, the structural load (i.e. $\overline{C_D}$ and $\overline{C_L'}$) on the I-shaped step cylinder with $l/D = 10$, 2 and 1.5 will be discussed. Then, the structural loads will be discussed for $l/D = 0.2$.

Figure 24(b,d) shows that the lift coefficient and the drag coefficient in the middle of the small cylinder for $l/D = 10$ are higher than for the single-step cylinder. This is because the symmetric shape of the I-step cylinder leads the S-cell vortex to shed in parallel behind the middle of the small cylinder for $l/D = 10$ (see figure 4a), while an oblique shedding angle of around 13 degrees was found for the single-step cylinder (Tian *et al.* 2023) at the same distance away from the step. This oblique vortex shedding will re-direct part of the spanwise vortex circulation (ω_z) into circulation in the other two directions. This will in turn decrease the base pressure strength, causing smaller structural load coefficients in the single-step cylinder case.

When l/D decreases from 10 to 2 (and 1.5), figure 24(b,d) shows that the distribution of $\overline{C_D}$ does not change significantly, while $\overline{C_L'}$ changes substantially along the small cylinder. The smaller $\overline{C_L'}$ as l/D decreases is due to the fact that the vorticity distribution in the near-wake region behind the small cylinder changes from asymmetric to almost symmetric (around the streamwise centre line) as l/D decreases from 10 to 2 (see figure 9a–f). During

https://doi.org/10.1017/jfm.2024.1103 Published online by Cambridge University Press

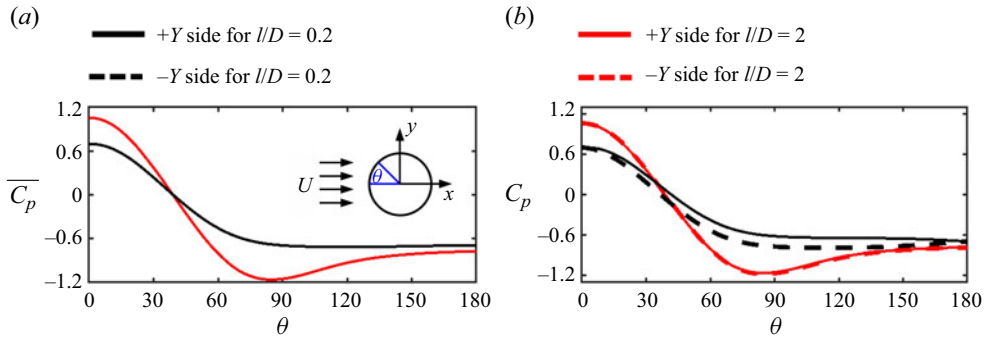

Figure 26. The circumferential distribution of pressure along a slice in the middle of the small cylinder at $z = 0$: (*a*) the time-averaged pressure and (*b*) the instantaneous pressure when C_L peaks at t1 (in figure 18*d*) for $l/D = 0.2$ and at t4 (in figure 9*h*) for $l/D = 2$. Notice that the continuous and broken lines coincide in (*a*).

this process, no clear decrease occurs in the magnitude of the spanwise vorticity $|\omega_z|$ (the dominant vorticity component in that region), leading to the almost unchanged $\overline{C_D}$.

As l/D further decreases from 2 to 0.2, $\overline{C_L'}$ increases and $\overline{C_D}$ decreases. Firstly, $\overline{C_D}$ is discussed in the light of the pressure on the $+X$ and $-X$ parts of the cylinder; figure 26(*a*) shows the circumferential distribution of the time-averaged pressure ($\overline{C_p} = 2(\bar{p} - p_0)$) along the small cylinder at $z = 0$ for $l/D = 2$ (red curve) and 0.2 (black curve). It appears that the time-averaged impinging pressure on the $-X$ part of the small cylinder ($\theta < 45$) and pressure on the $+X$ part of the small cylinder ($\theta > 90$) are weaker for $l/D = 0.2$ than for $l/D = 2$, leading to a smaller pressure difference between the $-X$ and the $+X$ parts of the cylinder, i.e. between fore and aft, and thus an overall smaller drag distribution along the small cylinder for $l/D = 0.2$ than for $l/D = 2$ (as shown in figure 24*b*). This is because the velocity surrounding the small cylinder is suppressed as the distance between the step surfaces decreases from $l/D = 2$ to $l/D = 0.2$, due to friction.

Secondly, $\overline{C_L'}$ is discussed in the light of the pressure on the $+Y$ and $-Y$ sides of the cylinder. Figure 26(*b*) shows the circumferential distribution of the instantaneous pressure along the small cylinder at $z = 0$ for $l/D = 2$ (red curve) and 0.2 (black curve) when C_L peaks for $l/D = 0.2$ (i.e. at t1 in figure 18*d*) and when C_L peaks for $l/D = 2$ (i.e. at t4 in figure 9*h*). It appears that the pressure difference between the $+Y$ and $-Y$ sides of the cylinder is visible for $l/D = 0.2$, but almost negligible for $l/D = 2$ when C_L peaks. Thus, the fluctuation amplitude of C_L for the $l/D = 0.2$ case is much larger than for $l/D = 2$, as shown in figures 9(*h*) and 18(*d*). This is due to the disappearance of the M-cell vortex and the appearance of the L-cell vortex behind the small cylinder, as l/D decreases from 2 to 0.2, which in turn makes the near wake change from symmetric to asymmetric, as shown by the vorticity contours in figures 9(*e–g*) and 18(*a–c*). This explains why $\overline{C_L'}$ is larger for $l/D = 0.2$ than for $l/D = 2$.

6. Conclusion

Flow over I-shaped step cylinders is investigated using DNS for $D/d = 2.0$ and $l/D = 10$, 5, 3, 2.5, 2, 1.5, 1 and 0.2 at $Re_D = 150$. As the length of the small cylinder l/D (i.e. the distance 'l' between the two steps) decreases from 10 to 0.2, four distinct wake modes (as shown in figure 4 and table 1) are identified behind the I-shaped step cylinder:

https://doi.org/10.1017/jfm.2024.1103 Published online by Cambridge University Press

(i) The F3SNL mode is identified for $l/D = 10$, 5 and 3. Here, '*SNL*' refers to the formation of the S-, N- and L-cell vortices, and '*F*3' indicates the corresponding three different shedding frequencies. It should be noted that these three vortex cells behave similarly to those behind the single-step cylinder. This is because, when the length of the small cylinder is large enough, the interaction between the two steps is almost negligible, making the wake behind an I-shaped step cylinder similar to the combination of two single-step cylinder wakes, except that the SS-half loop vortex behind the single-step cylinder becomes a closed S-S loop vortex behind the I-shaped step cylinder.

(ii) As l/D decreases to 2.5 and 2, the F2MNL mode is identified. Here, three dominant vortex cells, the M-, N- and L-cell vortices, appear but there are only two different shedding frequencies. Furthermore, the S-cell disappears and a new vortex structure, denoted the M-cell vortex, appears. The vanishing of the S-cell vortex is related to the distance between the steps: as the distance between the two steps becomes shorter, the wake mixing effect caused by the steps affects the flow over the whole small cylinder, thereby increasing the recirculation length. This suppresses the wake instability, causing the S-cell vortex to disappear. The reason why the M-, N- and L-cell vortices exhibit only two shedding frequencies is that all M-cell vortices shed in phase with the N-cell vortices.

(iii) As l/D further decreases to 1.5 and 1, the F3MNL mode is identified. Here, three dominant vortex cells, the M-, N- and L-cell vortices, appear and there are three distinct frequencies. The one additional shedding frequency (relative to the F2MNL mode) is due to the fact that the M-cell vortex starts to dislocate from the N-cell vortex, leading to the M-cell vortex exhibiting a different shedding frequency than the N-cell vortex. This is due to the following two reasons: (*a*) a decrease in l/D shortens the distance between the top and bottom N-cell vortices, leading to the M-cell vortex receiving more energy from the N-cell vortex. Thus, the M-cell vortices contain more circulation strength for the F3MNL mode than for the F2MNL mode. This stronger circulation strength makes the top and bottom parts of the M-cell vortex sustainable while disconnecting from the corresponding N-cell vortex. (*b*) The smaller blockage effect of the small cylinder (compared with the large cylinder) causes the averaged convective velocity to become larger behind the small cylinder (in the M-cell region) than behind the large cylinder region, contributing to a higher shedding frequency for the M-cell vortex than for the N-cell vortex.

(iv) The F1L mode is identified for $l/D = 0.2$. Here, the L-cell vortex becomes the only dominant vortex. The M-cell vortex vanishes because the small distance between the two steps highly suppresses the velocity surrounding the small cylinder, leading to a decrease of the circulation around the small cylinder, thus suppressing the formation of the M-cell vortex. The N-cell vortex disappears because the spanwise velocity and the varying suction pressure caused by the step become weak as the distance between the two steps (i.e. l/D) becomes very small.

Besides the wake flow, the streamwise vortex system around the I-shaped step cylinder was also investigated. Except for the case where the gap between the two steps becomes too small (e.g. $l/D = 0.2$), the streamwise vortex system around the I-shaped step cylinder is similar to that around the single-step cylinder, where a pair of edge vortices and a junction vortex occur. In the exceptional case, the junction vortex disappears due to the small gap between the two steps forcing the flow in between to become parallel.

https://doi.org/10.1017/jfm.2024.1103 Published online by Cambridge University Press

Investigations of the time-averaged drag coefficient ($\overline{C_D}$) and the root mean square of the lift coefficient ($\overline{C_L'}$) reveal that the distribution of the structural load along the I-shaped step cylinder significantly changes between the four identified wake modes. The results are directly compared with the structural load distribution along a corresponding single-step cylinder. For the F3SNL mode, the similar wake pattern behind the I-shaped step cylinder and the single-step cylinder gives rise to a similar distribution of $\overline{C_D}$ and $\overline{C_L'}$ along the I-shaped step cylinder and the single-step cylinder.

As the wake flow changes from the F3SNL mode to the F2MNL mode (and F3MNL mode), the staggered Kármán vortex shedding disappears behind the small cylinder. This causes the overall distribution of the lift force coefficient $\overline{C_L'}$ to significantly decrease on the small cylinder, as compared with the single-step cylinder. As the wake flow transforms to the F1L mode for $l/D = 0.2$, the wake behind both the small and large cylinders changes significantly. Along the large cylinder, the disappearance of the N-cell vortex causes the vortex dislocations between the N- and L-cell vortices to vanish, causing no local minimum (EX_{LL}) in the distribution of the lift coefficient ($\overline{C_L'}$). The distribution of $\overline{C_D}$ along the large cylinder for F1L is qualitatively similar to the other three modes: a local minimum EX_{DL} forms as the step is approached. However, the mechanism of the increased $\overline{C_D}$ from EX_{DL} to the step differs for F1L. As the multi-wake vortices change to the single wake vortex behind the I-shaped step cylinder from F3SNL, F2MNL and F3MNl to F1L, the non-monotonic distribution of the recirculation length along the larger cylinder changes to a monotonic distribution. This makes the enhanced pressure in the vicinity of the step on the large cylinder for F3SNL, F2MNL and F3MNl disappear for F1L, leading to the fact that the increased $\overline{C_D}$ from EX_{DL} to the step is caused by the pressure variation on the aft part of the cylinder for F3SNL, F2MNL and F3MNl; however, for F1L, the increased $\overline{C_D}$ is caused by the enhanced circumferential pressure on the fore part of the cylinder.

Behind the small cylinder in the F1L mode, the M-cell vortex disappears and the L-cell vortex appears. This converts the near wake of the small cylinder from symmetric to asymmetric (i.e. staggered) vortex shedding, thereby causing the overall distribution of $\overline{C_L'}$ to increase on the small cylinder, relative to the other three modes. The increased friction effect between the two steps for F1L compared with F3SNL, F2MNL and F3MNl weakens the pressure difference between the $-X$ and $+X$ sides of the small cylinder, leading to an overall smaller $\overline{C_D}$ for F1L than for the other three modes.

Acknowledgements. Computing resources were granted by the Norwegian Research Council (Program for Supercomputing) under projects nn9191k and nn9352k. Acknowledgements also go to L. Unglehrt, H. Strandenes and F. Jiang for their help and support in debugging and developing codes.

Declaration of interests. The authors report no conflict of interest.

Author ORCIDs.
Cai Tian https://orcid.org/0000-0001-7591-5617;
Jianxun Zhu https://orcid.org/0000-0002-5266-6125.

Appendix A. Grid convergence

As shown in § 3, the wake flow is more complex for the F2MNL and F3MNL modes than for the F3SNL and F1L modes due to the vortex interactions between the M- and N-cell vortices. Therefore, the I-shaped step cylinder with $l/D = 2$ where the F2MNL mode occurs is selected to conduct the grid convergence study. The three cases denoted

https://doi.org/10.1017/jfm.2024.1103 Published online by Cambridge University Press

Case	Min. cell size Δ_c/D	Domain size $(L_x \times L_y \times L_z)/D$	l/D	L/D	Grids ($\times 10^8$)
Fine 10	0.01	63.36 × 42.24 × 70.4	10	30.2	6.41
Fine 5	0.01	63.36 × 42.24 × 63.36	5	29.18	5.77
Fine 3	0.01	63.36 × 42.24 × 63.36	3	30.18	5.77
Fine 2.5	0.01	63.36 × 42.24 × 63.36	2.5	30.43	5.77
Coarse 2	0.015	60.48 × 40.32 × 60.48	2	29.24	1.51
Medium 2	0.012	62.208 × 41.472 × 62.208	2	30.104	3.19
Fine 2	0.01	63.36 × 42.24 × 63.36	2	30.68	5.77
Fine 1.5	0.01	63.36 × 42.24 × 63.36	1.5	30.93	5.77
Fine 1	0.01	63.36 × 42.24 × 63.36	1	31.18	5.77
Fine 0.2	0.01	63.36 × 42.24 × 63.36	0.2	31.58	5.77

Table 3. Mesh and computational domain information of all simulations in the present study. The case coarse has five levels of grids, and the other cases all have six levels of grids. The cases coarse 2, medium 2 and fine 2 are used for the grid study. As shown in figure 2, the minimum grid cells (Δ_c/D) cover the close region around the I-shaped step cylinder.

Grid	—	Level 6	Level 5	Level 4	Level 3	Level 2
Fine 2	x	(−0.88, 2.20)	(−1.32, 5.28)	(−1.76, 7.92)	(−3.52, 10.56)	(−7.04, 14.08)
	y	(−0.88, 0.88)	(−1.32, 1.32)	(−1.76, 1.76)	(−3.52, 3.52)	(−7.04, 7.04)
Medium 2	x	(−0.864, 2.592)	(−1.296, 5.184)	(−1.728, 7.775)	(−3.456, 10.368)	(−6.912, 13.824)
	y	(−0.864, 0.864)	(−1.296, 1.296)	(−1.728, 1.728)	(−3.456, 3.456)	(−6.912, 6.912)
Coarse 2	x	(−0.84, 2.52)	(−1.26, 5.04)	(−1.68, 7.56)	(−3.36, 10.08)	(−6.72, 13.44)
	y	(−0.84, 0.84)	(−1.26, 1.26)	(−1.68, 1.68)	(−3.36, 3.36)	(−6.72, 6.72)

Table 4. Locations of the grid-refinement regions for the original case and the case with an increased grid-refinement region. All the grid-refinement regions occupy the whole flow domain in the z-direction. The level 1 grid covers the whole flow domain.

Case	$St_M = St_N$	St_L
Coarse 2	0.153	0.173
Medium 2	0.154	0.175
Fine 2	0.155	0.175

Table 5. The St of three dominant vortex cells ($St_M = f_M D/U$, $St_N = f_N D/U$ and $St_L = f_L D/U$) for the three cases with $l/D = 2.0$, i.e. coarse 2, medium 2 and fine 2, as shown in table 3.

coarse 2, medium 2 and fine 2 (shown in table 3) are set up for the grid convergence study. The locations of the grid-refinement region for the coarse 2, medium 2 and fine 2 cases is shown in table 4.

The St of the three dominant vortex cells ($St_M = f_M D/U$, $St_N = f_N D/U$ and $St_L = f_L D/U$) is calculated by FFT of the time series of the streamwise velocity u along a vertical sampling line at $(x, y) = (1.6, 0.4)$ for coarse 2, medium 2 and fine 2. The results are shown in table 5, indicating tiny differences for the St in these three cases.

Figure 27(a,b) shows the time-averaged streamwise velocity ($\bar{u}$) and pressure ($\bar{p}$) along the sampling line AB (see in figure 27a-ii) located upstream of the small cylinder at $(x, y) = (-0.4, 0)$, respectively. A close-up of the red rectangle in figure 27(a,b) is shown in figures 27(a-i) and 27(b-i), respectively, indicating a convergent tendency from the

https://doi.org/10.1017/jfm.2024.1103 Published online by Cambridge University Press

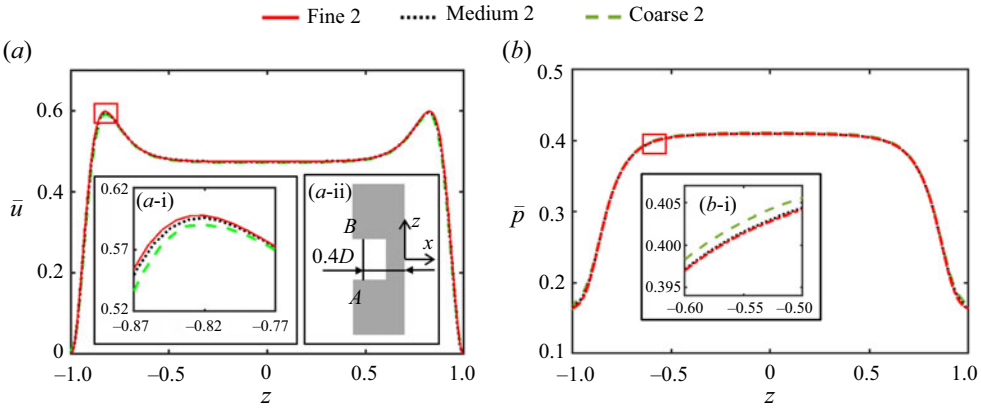

Figure 27. (*a*) Distributions of time-average streamwise velocity $\bar{u}$ along a sampling line AB in the *xz*-plane at $y = 0$ in the $l/D = 2$ case. Inset: (*a*-i) a zoomed-in view of the upper part of the curves (red rectangle in *a*); (*a*-ii) a sketch of the position of the sampling line AB of length $2D$ at $x = -0.4$. (*b*) Distribution of time-averaged pressure $\bar{p}$ along a sampling line AB. Inset: (*b*-i) a zoomed-in view of the upper part of the curves (red rectangle in *b*).

coarse 2 case to the fine 2 case. The difference between medium 2 and fine 2 is negligible. The above comparisons indicate that the grid resolution in the fine 2 case is sufficiently fine to accurately simulate the flow around the I-shaped step cylinders discussed in the present paper. Grid and computational domain information of all simulations in the present study are shown in table 3.

The horizontal size of the computational domain (L_x and L_y shown in table 3 and figure 3) applied in the present study is larger than that used by Morton & Yarusevych (2010), Tian *et al.* (2023) and Massaro *et al.* (2023*b*) and comparable to that applied by Tian *et al.* (2021) for the single-step cylinder at the same or higher Re_D. The spanwise convergence study provided by Tian *et al.* (2023) shows that a $45D$ step cylinder ($30D$ for the large cylinder and $15D$ for the small cylinder) can make the free-slip boundary condition used at the top and bottom boundaries have a minor effect on the flow region around the step spanning in $20D$ for flow over a single-step cylinder with $D/d = 2$ at $Re_D = 150$. Considering that the I-shaped step cylinder applied in the present study has the same diameter ratio ($D/d = 2$) and Reynolds number ($Re_D = 150$), the length of the large cylinder L is set up to around $30D$ for all cases with the length of the small cylinder varying from 0.2 to 10, as shown in table 3.

Appendix B. Wake overview for $l/D = 5, 3, 2.5, 1.0$

This appendix includes four figures, i.e. figures 28, 29, 30 and 31. All vortex structures are visualized by instantaneous isosurface of $\lambda_2 = -0.01$. All velocity spectra are calculated by a FFT of at least $1500D/U$ continuous streamwise velocity (u) data along a vertical sampling line parallel to the z-axis at $(x, y) = (1.6, 0.4)$.

https://doi.org/10.1017/jfm.2024.1103 Published online by Cambridge University Press

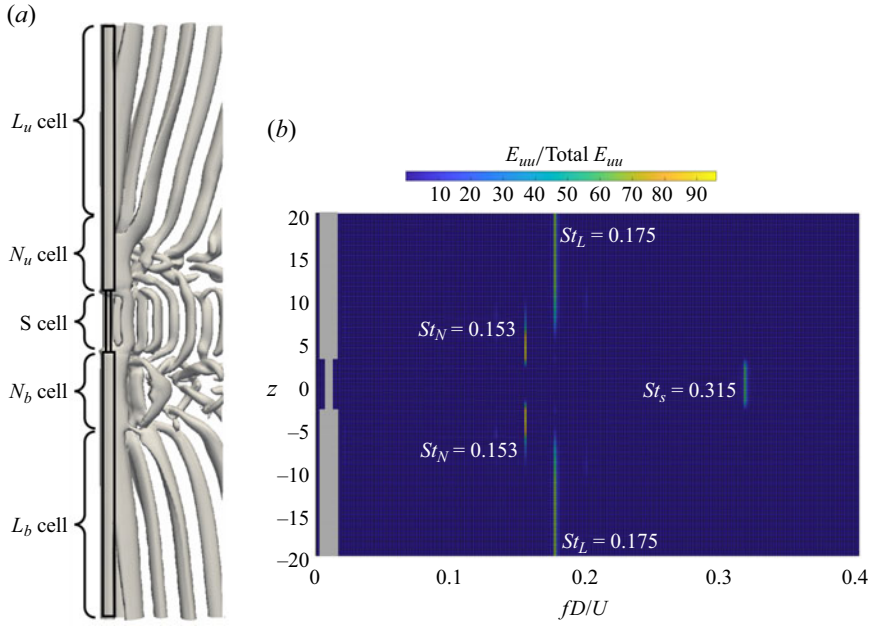

Figure 28. (*a*) Instantaneous isosurface of $\lambda_2 = -0.01$ for $l/D = 5$. (*b*) The corresponding streamwise velocity spectrum is obtained from a FFT of time series of the streamwise velocity u along a vertical sampling line behind the I-shaped step cylinder at $(x, y) = (1.6, 0.4)$.

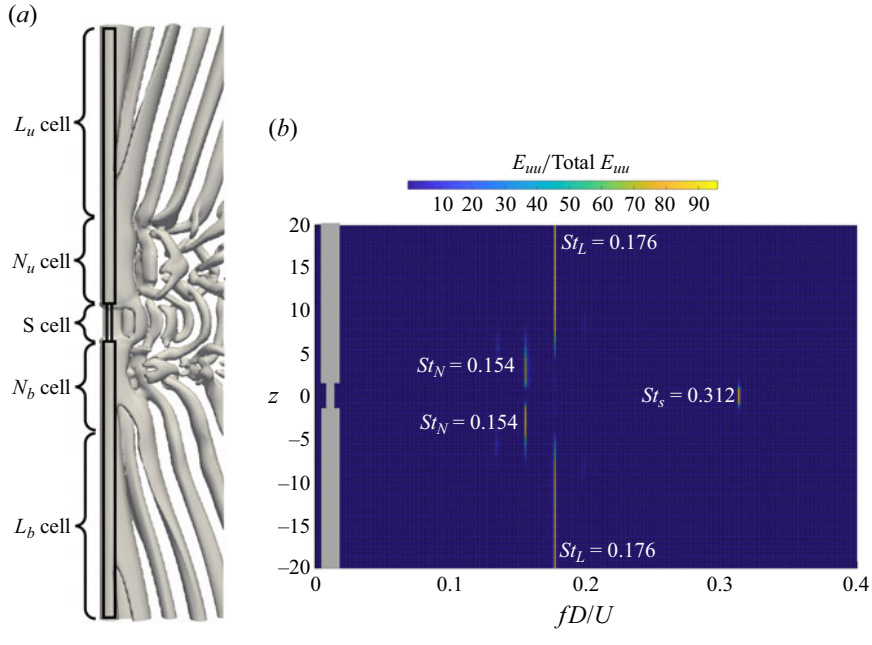

Figure 29. Same as figure 28, but for $l/D = 3$.

https://doi.org/10.1017/jfm.2024.1103 Published online by Cambridge University Press

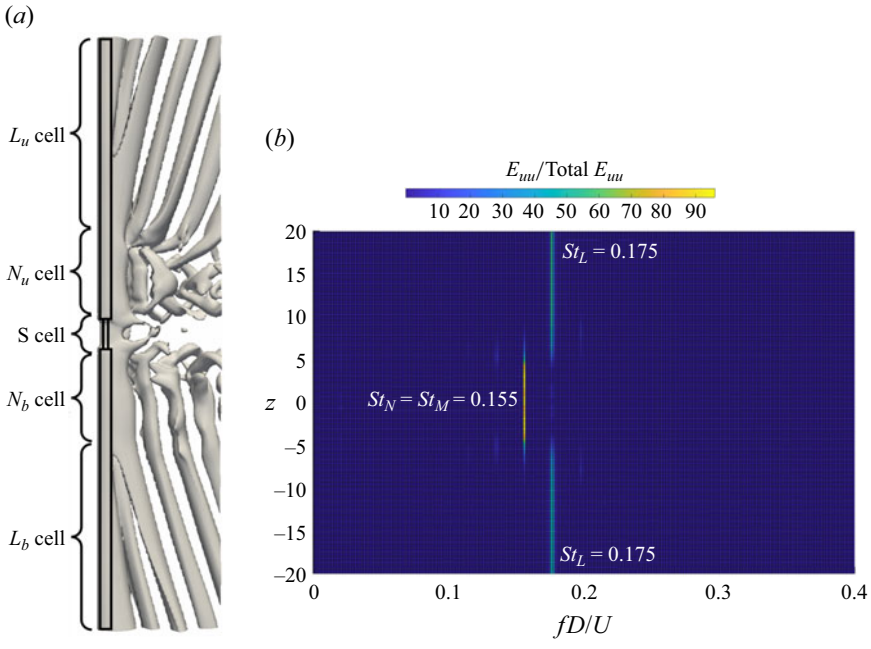

Figure 30. Same as figure 28, but for $l/D = 2.5$.

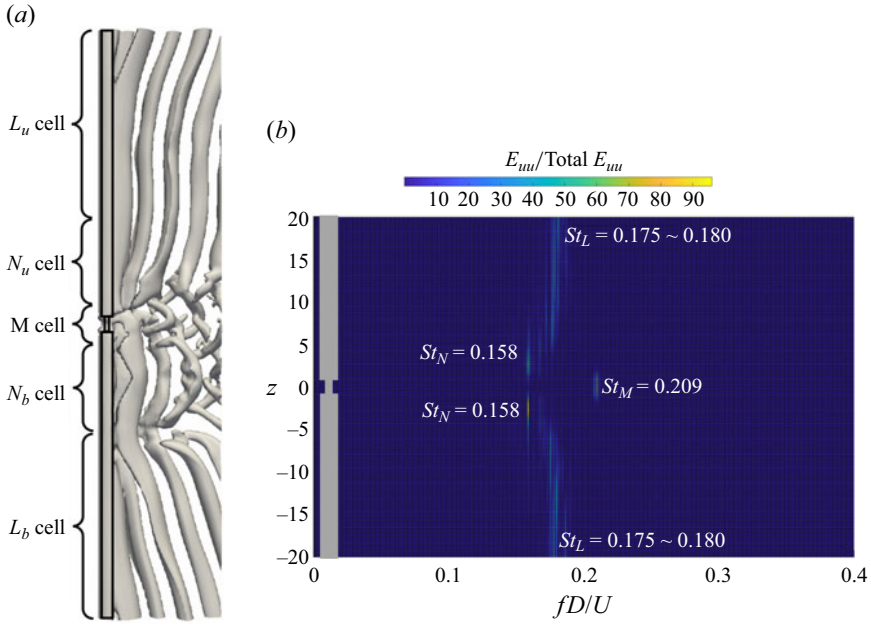

Figure 31. Same as figure 28, but for $l/D = 1$.

https://doi.org/10.1017/jfm.2024.1103 Published online by Cambridge University Press

References

Bulbule, S., Kumar, P. & Singh, S.K. 2024 Investigation of wake dynamics near the cylinder with the variation of length-to-diameter ratio. *Phys. Fluids* **36** (8), 085162.

Dunn, W. & Tavoularis, S. 2006 Experimental studies of vortices shed from cylinders with a step-change in diameter. *J. Fluid Mech.* **555**, 409–437.

Jayavel, S. & Tiwari, S. 2009 Numerical study of heat transfer and pressure drop for flow past inline and staggered tube bundles. *Intl J. Numer. Meth. Heat Fluid Flow* **19** (8), 931–949.

Jeong, J. & Hussain, F. 1995 On the identification of a vortex. *J. Fluid Mech.* **285**, 69–94.

Ji, C., Yang, X., Yu, Y., Cui, Y. & Srinil, N. 2020 Numerical simulations of flows around a dual step cylinder with different diameter ratios at low Reynolds number. *Eur. J. Mech.* B/*Fluids* **79**, 332–344.

Jiang, F., Pettersen, B., Andersson, H.I., Kim, J. & Kim, S. 2018 Wake behind a concave curved cylinder. *Phys. Rev. Fluids* **3** (9), 094804.

Ko, N.W.M. & Chan, A.S.K. 1984 Pressure distributions on circular cylinders with stepwise change of the diameter. In *ASME Paper*, pp. 84–WA/FE–13. ASME.

Lewis, C.G. & Gharib, M. 1992 An exploration of the wake three dimensionalities caused by a local discontinuity in cylinder diameter. *Phys. Fluids* A **4**, 104–117.

Manhart, M. 2004 A zonal grid algorithm for DNS of turbulent boundary layers. *Comput. Fluids* **33**, 435–461.

Massaro, D., Peplinski, A. & Schlatter, P. 2023*a* Coherent structures in the turbulent stepped cylinder flow at $Re = 5000$. *Intl J. Heat Fluid Flow* **102**, 109144.

Massaro, D., Peplinski, A. & Schlatter, P. 2023*b* The flow around a stepped cylinder with turbulent wake and stable shear layer. *J. Fluid Mech.* **977**, A3.

Massaro, D. & Schlatter, P. 2024 Global stability of the flow past a stepped cylinder. *J. Fluid Mech.* **988**, A1.

Matsumoto, M., Shiraishi, N. & Shirato, H. 1992 Rain-wind induced vibration of cables and cable-stayed bridges. *J. Wind Engng Ind. Aerodyn.* **43** (1), 2011–2022.

Morton, C. & Yarusevych, S. 2010 Vortex shedding in the wake of a step cylinder. *Phys. Fluids* **22** (8), 083602.

Morton, C. & Yarusevych, S. 2014*a* On vortex shedding from low aspect ratio dual step cylinders. *J. Fluids Struct.* **44**, 251–269.

Morton, C. & Yarusevych, S. 2014*b* Vortex dynamics in the turbulent wake of a single step cylinder. *J. Fluids Engng* **136** (3), 031204.

Morton, C. & Yarusevych, S. 2020 Vortex shedding from cylinders with two step discontinuities in diameter. *J. Fluid Mech.* **902**, A29.

Morton, C., Yarusevych, S. & Carvajal-Mariscal, I. 2009 Study of flow over a step cylinder. *Appl. Mech. Mater.* **15**, 9–14.

Nakamura, H. & Igarashi, T. 2008 Omnidirectional reductions in drag and fluctuating forces for a circular cylinder by attaching rings. *J. Wind Engng Ind. Aerodyn.* **96** (6–7), 887–899.

Peller, N. 2010 Numerische simulation turbulenter strömungen mit immersed boundaries. PhD thesis, Technical University of Munich, Germany.

Peller, N., Duc, A.L., Tremblay, F. & Manhart, M. 2006 High-order stable interpolations for immersed boundary methods. *Intl J. Numer. Meth. Fluids* **52**, 1175–1193.

Rajani, B.N., Kandasamy, A. & Majumdar, S. 2009 Numerical simulation of laminar flow past a circular cylinder. *Appl. Math. Model.* **33** (3), 1228–1247.

Schanderl, W., Jenssen, U., Strobl, C. & Manhart, M. 2017 The structure and budget of turbulent kinetic energy in front of a wall-mounted cylinder. *J. Fluid Mech.* **827**, 285–321.

Stone, H.L. 1968 Iterative solution of implicit approximations of multidimensional partial differential equations. *SIAM J. Numer Anal.* **5**, 530–558.

Theja, C., Sathia, K.R., Mahesh, S. & Narasimhamurthy, V.D. 2024 Large eddy simulation of turbulent wake from dual-step cylinders. *Phys. Fluids* **36** (10), 105163.

Tian, C., Jiang, F., Pettersen, B. & Andersson, H.I. 2017*a* Antisymmetric vortex interactions in the wake behind a step cylinder. *Phys. Fluids* **29** (10), 101704.

Tian, C., Jiang, F., Pettersen, B. & Andersson, H.I. 2017*b* Numerical investigation of flow around a step cylinder. In *Proceedings of 9th National Conference on Computational Mechanics, Trondheim, Norway, 11–12 May*, pp. 369–384. CIMNE.

Tian, C., Jiang, F., Pettersen, B. & Andersson, H.I. 2019 The long periodicity of vortex dislocations in the wake behind a step cylinder. In *Proceedings of 10th National Conference on Computational Mechanics, Trondheim, Norway, 3–4 June*, pp. 81–99. CIMNE.

https://doi.org/10.1017/jfm.2024.1103 Published online by Cambridge University Press

TIAN, C., JIANG, F., PETTERSEN, B. & ANDERSSON, H.I. 2020*a* Diameter ratio effects in the wake flow of single step cylinders. *Phys. Fluids* **32** (9), 093603.

TIAN, C., JIANG, F., PETTERSEN, B. & ANDERSSON, H.I. 2020*b* Vortex dislocation mechanisms in the near wake of a step cylinder. *J. Fluid Mech.* **891**, 393–441.

TIAN, C., JIANG, F., PETTERSEN, B. & ANDERSSON, H.I. 2021 Vortex system around a step cylinder in a turbulent flow field. *Phys. Fluids* **33** (4), 045112.

TIAN, C., ZHU, J., HOLMEDAL, L.E., ANDERSSON, H.I., JIANG, F. & PETTERSEN, B. 2023 How vortex dynamics affects the structural load in step cylinder flow. *J. Fluid Mech.* **972**, A10.

UNGLEHRT, L. & MANHART, M. 2022 Onset of nonlinearity in oscillatory flow through a hexagonal sphere pack. *J. Fluid Mech.* **944**, A30.

WILLIAMSON, C.H.K. 1989 Oblique and parallel modes of vortex shedding in the wake of a circular cylinder at low Reynolds numbers. *J. Fluid Mech.* **206**, 579–627.

WILLIAMSON, J.H. 1980 Low-storage Runge–Kutta schemes. *J. Comput. Phys.* **35**, 48–56.

YIN, D., LIE, H. & WU, J. 2020 Structural and hydrodynamic aspects of steel lazy wave riser in deepwater. *Trans. ASME J. Offshore Mech. Arctic Engng* **142**, 020801.

YU, Y., JI, C. & SRINIL, N. 2020 Three-dimensional flip-flopping flow around a pair of dual-stepped circular cylinders in a side-by-side arrangement. *Phys. Fluids* **32** (12), 123608.

ZHAO, M. & ZHANG, Q. 2023 Three-dimensional numerical simulation of flow past a rotating step cylinder. *J. Fluid Mech.* **962**, A45.

https://doi.org/10.1017/jfm.2024.1103 Published online by Cambridge University Press